Chapter 3. Mechanisms driving brines within the NEGB. Results from 2D coupled fluid flow-mass transport and thermohaline simulations

In this chapter the various components involved in brine transport within the NEGB are described. For this purpose, the chapter has been structured in two parts. In the first part, diffusive brine transport is studied. Subsequently, the advective mass flux induced by topography-driven fluid flow (variable hydraulic head) is also taken into account. In the second part, temperature effects are investigated by simulating thermohaline convection. When the regional flow is excluded or included in the thermohaline model the regime is respectively referred to as free or mixed convection. In order to allow mass and heat outflow through the surface, open boundary conditions for fluid concentration and temperature are defined. Initial conditions for head, mass and temperature distribution are those illustrated in Chapter 2, paragraph 2.2.2.

The evolution of temperature and mass patterns are shown at two time steps. In all the pictures, the label "A" and "B" refer to a computing time of $t = 30$ ka and $t = 200$ ka respectively. It is worth recall that these time steps are not referred to any geological timescales but present computing time (paragraph 2.2.3). Accordingly, the patterns shown here depict "snapshots" in time. The results will indicate the possible mechanisms leading to near-surface salt water occurrences.

3.1 Diffusive brine transport

In this first part, the heat flux balance equation (Eq.(2.4)) is not solved since temperature gradients are neglected. Therefore, the EOS for the fluid density (Eq.2.6)) is a function of pressure and concentration with no temperature dependency (i.e. $\beta = 0$).

3.1.1 Boundary conditions

The boundary conditions defined for the diffusive brine transport problem are the following:

- The surface is permeable to solute outflow while the head boundary conditions will be discussed separately in the next paragraphs for the case in which the regional flow is excluded or included in the model.
- At the Top Salt a fixed concentration value of 345.2 g/L is set,
- The lateral boundaries are closed to fluid and mass flow.

In the NEGB the advected solute can flow out of the basin through the upper surface. For that reason, an open boundary condition allowing solute outflow (i.e. permeable) is needed at the top surface of the model domain. This boundary condition, referred to as Cauchy type boundary condition, is defined by the following relation:

$$\mathbf{q}_{\mathbf{C}}(t) = -\Phi_{\mathrm{C}}(C^{*} - C)\mathbf{n} \tag{3.1}$$

where $\mathbf{q}_{\mathbf{C}}$ is the solute flux, Φ_{C} is a mass transfer coefficient, C^{*} is the prescribed boundary condition value for the solute concentration C at the surface, and $\mathbf{n}$ is the vector normal to the top surface of the domain. By setting a natural boundary condition for the solute at the top slice of the model, the concentration C is solved at each node of the boundary: a solute flow through the top surface of the domain is computed. The transfer coefficient Φ_{C} appearing in Eq.(3.1) can be regarded as a leaching parameter which governs the mass flux through the boundary. The two limiting cases for Φ_{C} are $\Phi_{\mathrm{C}} = 0$ and $\Phi_{\mathrm{C}} \to \infty$. In the first case, the surface is impervious to solute flux since $\mathbf{q}_{\mathbf{C}} = 0$. For a very large value of Φ_{C}, $C \to C^{*}$ and therefore the Cauchy boundary condition is reduced to a Dirichlet-type. The mass transfer is a numerical coefficient allowing the definition of an open boundary condition in the form of Eq.(3.1) rather than a real measurable parameter. Nevertheless a reasonable value of the mass transfer coefficient can be estimated by rewriting Eq.(3.1) in a Fickian form, viz.:

$$q_{\mathrm{C}}(t) \approx -D_{\mathrm{leak}} \frac{C^{*} - C}{d} \tag{3.2}$$

where d is the thickness of a thin stratum in contact with the top surface of the domain through which the solute leaches. The mass transfer coefficient then becomes:

$$\Phi_{\mathrm{C}} \approx \frac{D_{\mathrm{leak}}}{d} \quad \text{in} \quad \left[ms^{-1}\right] \tag{3.3}$$

where D_{leak} is a representative molecular diffusion coefficient of the thin stratum. D_{leak} can be considered more or less equal to the molecular diffusivity of the bordering stratigraphic unit (i.e. Cenozoic, $D_{leak} \approx 2 \times 10^{-9}\ ms^{-2}$ Table 1.1). A stratum thickness in the range of a meter can be regarded as relatively thin with respect to the basin scale. Hence, from Eq.(3.3) $\Phi_C \approx 2 \times 10^{-9}\ ms^{-1}$. The prescribed surface boundary condition C^* has been set equal to the reference concentration value, i.e. $C^* = 0$ g/L.

3.1.2 Diffusive brine transport without regional flow

In this paragraph, the regional flow is not taken into account in the simulation of brine transport. By ignoring topography-induced fluid flow the resulting brine patterns are not affected by advective flux and salt dissolution is not enhanced by any external factor. Therefore the major sources of salinity can be directly inferred.

In order to exclude the regional flow from the simulation, the head has been referred to a constant value of 25 m at the upper boundary. This value corresponds to the minimum surface elevation of the study area so that the head level cannot exceed the topography.

Fig.3-1 A, B illustrate the resulting mass patterns at the computing time of 30 ka and at the end of the simulation run ($t = 200$ ka) respectively. In these figures a 10:1 vertical exaggeration is used. P1 and P2 indicate two profiles in which the results will be illustrated afterwards with no vertical exaggeration. At $t = 30$ ka (Fig.3-1 A) brine plumes with 1 g/L form on the salt diapirs crest and sinks along the domes flanks into the deeper sediments. Additionally, a strong concentration gradient develops within the whole Buntsandstein unit. The concentration values range from 200 g/L at its surface to 345 g/L which is the halite fluid saturation at the top salt. The interface fresh water/brine is well defined and located above the Buntsandstein surface within the Muschelkalk. This feature is explained as follows: starting from the initial mass concentration, a transition zone between fresh water and highly concentrated brine diffuses throughout the Buntsandstein as a result of salt dissolution. Due to its very low permeability, the Muschelkalk inhibits the motion and sharply shapes the interface of this transition zone. Accordingly, a very high concentration gradient is formed within this unit. At $t = 200$ ka (Fig.3-1 B) the salt distribution within the Buntsandstein remains unchanged which proves that a steady concentration gradient has been reached herein. On the other hand, above the Buntsandstein, dissolved halite continues diffusing in the neighbourhood of salt domes. Layered brine plumes spread at both sides of the salt diapirs (Fig.3-1 B). The salt dome environment is hydrologically unique, i.e. groundwater is

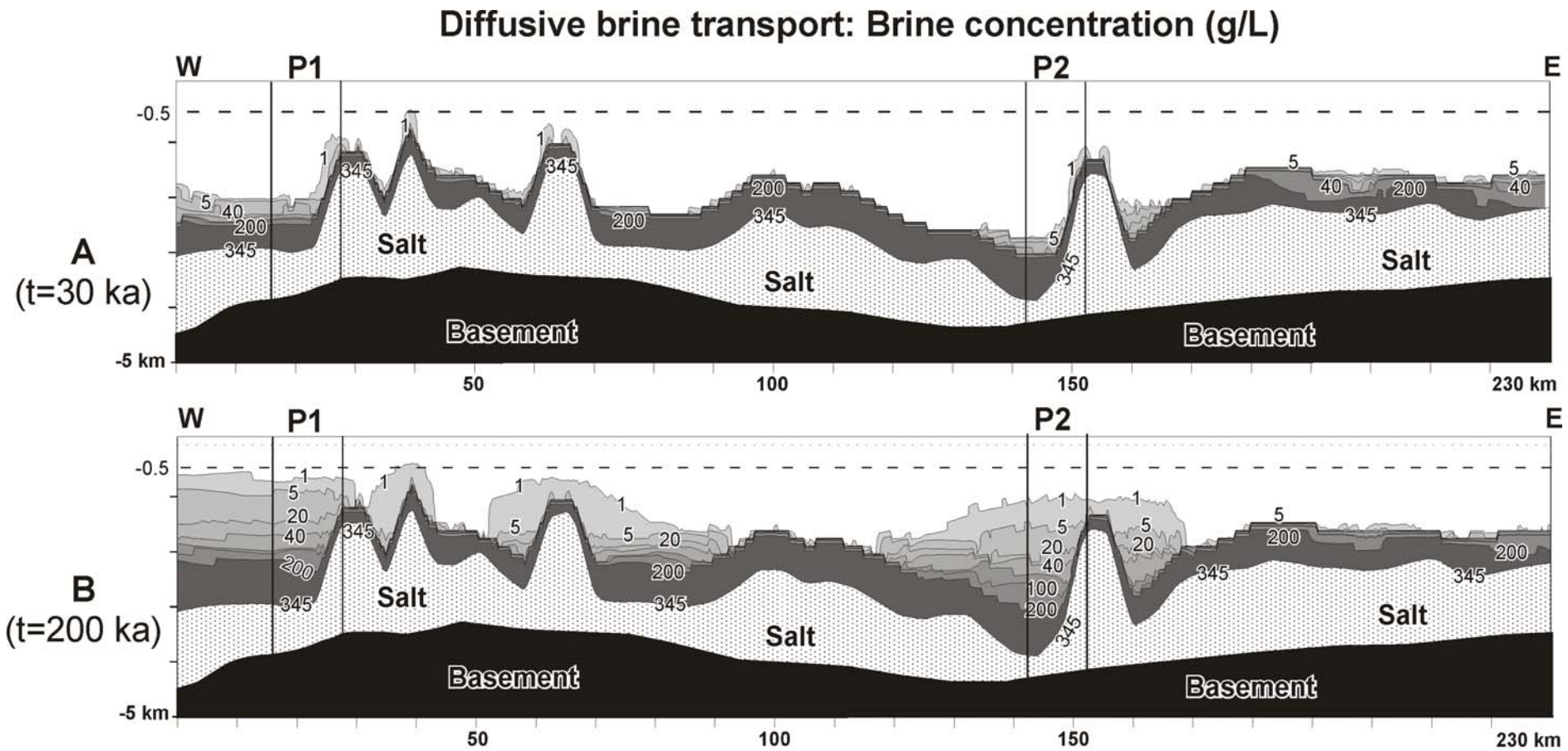

Fig.3-1: **A and B** mass distribution resulting from coupled fluid flow and mass transport simulation at $t = 30$ ka and $t = 200$ ka respectively. The regional flow is excluded from the numerical computation. Salt concentrations are expressed in g/L. The snapshots are interpolated by the use of Surfer 8® and illustrated with a 10:1 vertical exaggeration. Two profiles P1 and P2 are located within the cross-section. The simulation results for these two profiles are shown with no vertical exaggeration in Fig.3.2 and Fig.3.3

subjected to large lateral salinity gradients. Along salt dome flanks the density gradient drives groundwater flow laterally into the basin. The dissolved halite spreads away from salt bodies by diffusion and increases rapidly the salinity of the pore water throughout the sediments. The resulting brine plumes extend over 30 km in the lateral directions. As a result, dissolved halite concentration around salt domes increases with depth. Above salt diapir crests, brackish water with 1 g/L of dissolved salt can reach a depth between one and half kilometre. Far from salt domes, the salty plumes do not develop as it is the case in the central and eastern part of the basin.

In Fig.3-2 A, B the velocity field (label 1) and the formation of brine (label 2) are illustrated along the diapir "P1". No vertical exaggeration is used and two simulation stages are depicted (label A: $t = 30$ ka , label B: $t = 200$ ka). Brine density flow develops rapidly and the highly concentrated salty groundwater forming near the flank of the diapir sinks due to gravity (Fig.3-2 A). Downward brine flow generates a clockwise convective cell of fresh water above the salt dome which recharges the sediments (Fig.3-2 A1). After 30 ka, the pore velocities range from 2 cm yr^{-1} to few millimeters per year. Maximum flow velocity occurs adjacent to the dome edge. By comparing Fig.3-2 A with Fig.3-2 B it turns out that, as time progresses, the velocities decrease and the convective cell breaks apart (Fig.3-2 B1). This occurs since halite diffuses from the salt flanks into the overlying sediments and brines fill up more of the sediments surrounding the salt dome (Fig.3-2 B2). Peak velocities still occur along the salt diapirs flank. Since a constant salt concentration is used as boundary condition for the solute at the salt surface there is a lateral density gradient at all times near the salt dome. Therefore, downward solute motion continues even after the surrounding sediments are filled with brine. The observations pertaining to this salt dome environment hold for all salt domes present in the section. For the sake of completeness, velocities and mass patterns are also shown for another salt flank in Fig.3-3. The location is indicated with "P2" in Fig.3-1. At the beginning of the process, a fresh water convective cell forms above the salt dome as a result of dissolved halite sinking along the salt flanks (Fig 3.3 A1). The pore velocities span the same range as in profile 1, i.e. from 2 cm yr^{-1} to few millimeters per year. At the end of the simulation process, sediments are filled with more brine and flow velocities decrease (Fig.3-3 B). All the described features have also been attained by Evans et al. (1991), who investigated the mechanisms driving groundwater flow near salt domes.

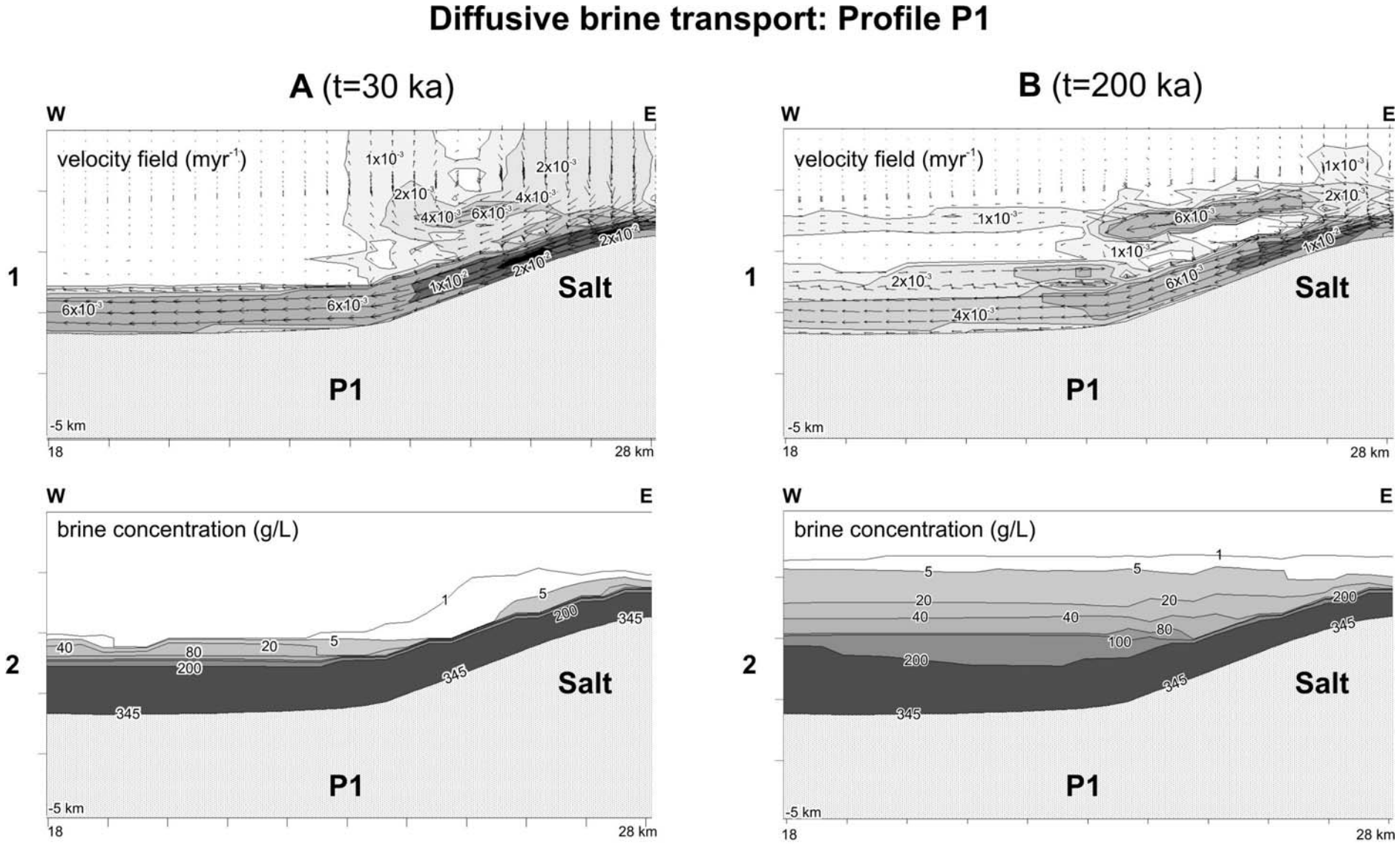

Fig.3-2: **A and B:** Zoom of the diffusive brine transport simulation results for profile P1 as located in Fig.3.1 at $t = 30$ ka and at $t = 200$ ka respectively. No vertical exaggeration is used. **1:** pore water velocity field in myr^{-1}. Pore vector linearly scaled to the largest flow arrow. **2:** Salt concentration distribution in g/L.

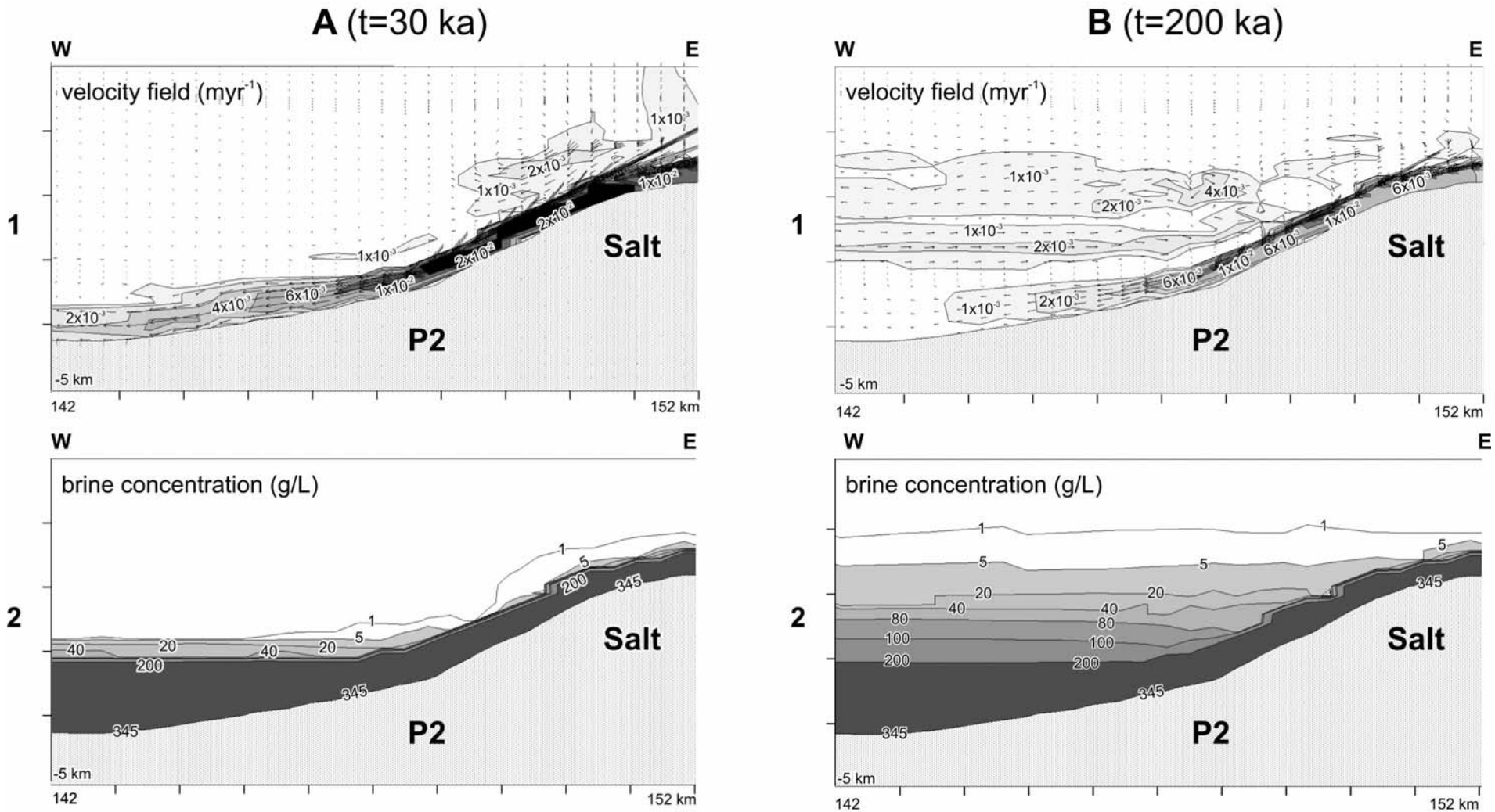

Fig.3-.3: **A and B:** Zoom of the diffusive brine transport simulation results for profile P2 as located in Fig.3.1 at $t = 30$ ka and $t = 200$ ka . No vertical exaggeration is used. **1:** pore water velocity field in myr^{-1} . Pore vector linearly scaled to the largest flow arrow. Pore vector linearly scaled to the largest flow arrow. **2:** Salt concentration distribution in g/L

In summary, the numerical results show that in the Buntsandstein a steady state concentration profile is already achieved at an early simulation stage ($t = 30$ ka). As time progresses, the mass pattern within this unit does not undergo significant variation. On the other hand, around the salt diapirs, halite continues diffusing and salty water fills the surrounding sediments in the lateral direction. In salt dome environments, active halite dissolution occurs and density driven fluid flow is the major transport mechanism. Steep salt structures supply a continuous halite replenishment. Downward motion of dissolved halite, due to the gravity, is dominant along salt flanks. The calculated velocity peak is 2 cm yr^{-1}. The resulting drag forces generate localized convective cells in the overlying sediments which provides the main recharge of fresh water. As heavier salt-laden water is produced, velocities decrease and the convective cells weaken or disappear. Brackish water with 1 g/L of dissolved salt occurs at depths between half and 1 km in the surrounding of shallow salt structures.

3.1.3 Diffusive brine transport and regional flow

Numerous factors influence the transport of salt and groundwater flow near salt domes. In sedimentary basins, forced advective flux provided by the regional flow cannot be overlooked (Bodenlos 1970; Posey and Kyle 1988). Regional flow enhances fluid circulation due to the viscous drag, promotes salt dissolution and extend salinity plumes away from the salt domes (Evans et al. 1991). As mentioned in paragraph 1.2.3, the fresh meteoric water infiltrates into the sediments induced by topographical variation. The mixing processes between regional and groundwater flow are supposed to reach approximately a depth of half a kilometer. In the NEGB most of the salt domes penetrate nearly to the basin surface and therefore are exposed to, and affected by topography-driven inflow of fresh water.

Numerically, the regional flow is taken into account by setting the head level equal to the topographic relief. Under these hydraulic boundary conditions, groundwater recharges the basin in the highlands while discharge areas occur in the lowlands. The rate of flow is controlled by the topographic relief and the patterns of flow mostly by the permeability, and the geometry of the stratigraphic units. Fig.3-4 (1) illustrates the regional flow patterns together with the computed velocity field. The stratigraphic units of the cross section are shown below (Fig.3-4 2). In the shallow aquifer (i.e. down to 500 m depth) the fluid flow direction is schematically represented by bold arrows while dashed arrows are used for the deeper part of the basin. The more intense regional flow is confined in the Cenozoic unit where the sediments have the highest hydraulic conductivity.

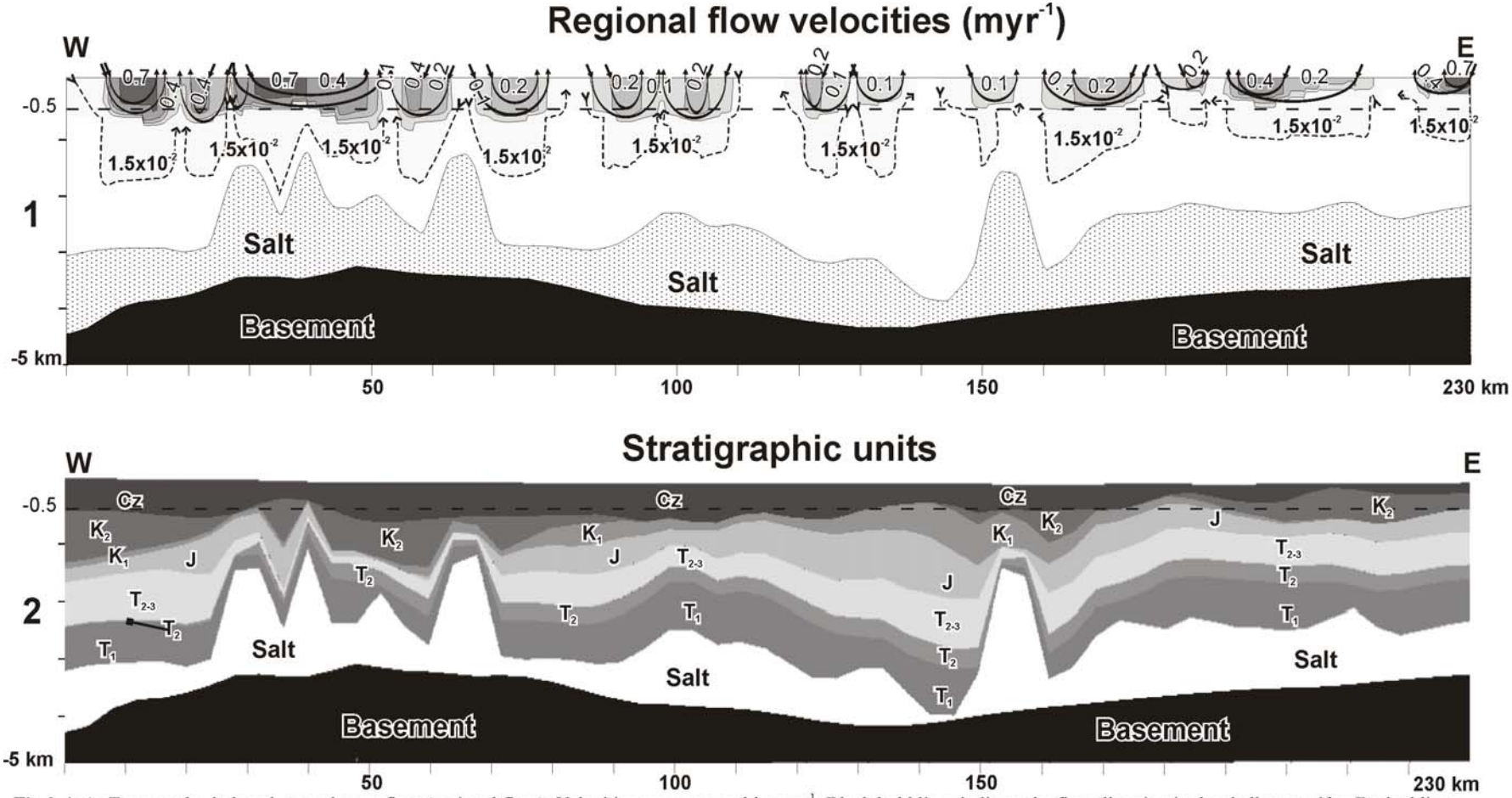

Fig.3-4: **A:** Topography-induced groundwater flow (regional flow). Velocities are expressed in myr^{-1}. Black bold lines indicate the flow direction in the shallow aquifer. Dashed lines depict the flow circulation in the deeper part of the basin. **B:** Geological structure (stratigraphic units abbreviations in Table 1.1)

The fluid velocities range from 0.7 m yr^{-1} to 0.1 m yr^{-1} whereas at a depth of 2 km fluid motion occurs at a velocity of few centimeters per year. These strong variations in the velocity range reflect the high heterogeneity of the sediments.

The calculated mass distribution is illustrated in Fig.3-5 A, B at the beginning and at the end of the simulation process ($t = 30$ ka and $t = 200$ ka respectively). The regional fluid flow streamlines (as shown in Fig.3-4) are depicted as well. At $t = 30$ ka (Fig.3-5 A) the Buntsandstein is saturated with heavy brine, as already discussed in the previous paragraph. On the other hand, at the western part of the basin, the concentration isopleths are convex: salt water upwelling begins near the salt dome. An elongated plume of brackish water is found in association with upward fluid motion supplied by the topography-induced flow. As time progresses, the salty plume extends up to the surface (Fig.3-5 B). Brackish water with more than 1 g/L of salt spreads in the discharge area. Throughout the rest of the basin, brine transport is also strongly affected by regional fluid circulation in the neighborhood of salt domes. Salt downwellings (concave solutal isopleths) occur where fluid descend in the basin since fresh water infiltrates into the sediments. On the other hand, salt upconings (convex solutal isopleths) arise where fluid ascends. Nevertheless no brine outflow occurs with the exception of the western part of the basin where brine leaches through the surface. In general, the salty plumes reach a depth of approximately half a kilometer. The causes leading to surface salt occurrence in the western part of the basin can be inferred by observing the regional flow intensity (Fig.3-4 (1)) and the mass patterns resulting from salt diffusion (Fig.3-1). At the western part of the basin, groundwater is released at high velocities (Fig.3-4 (1)). Moreover, in that area of the basin, shallow salt dissolution is favored (Fig.3-1 B). As a result, the regional flow discharges in the lowlands at rates high enough to advect dissolved halite close to the surface. The brackish water leaches through the sediments and spreads at the surface.

In order to gain insights into the influence of topography-induced flow on salt transfer, the velocity field of the regional flow and the calculated salt concentrations are illustrated with no vertical exaggeration in two areas of the basin. The two profiles P3 and P4 associated with salt domes are indicated on the cross-section in Fig.3-5.

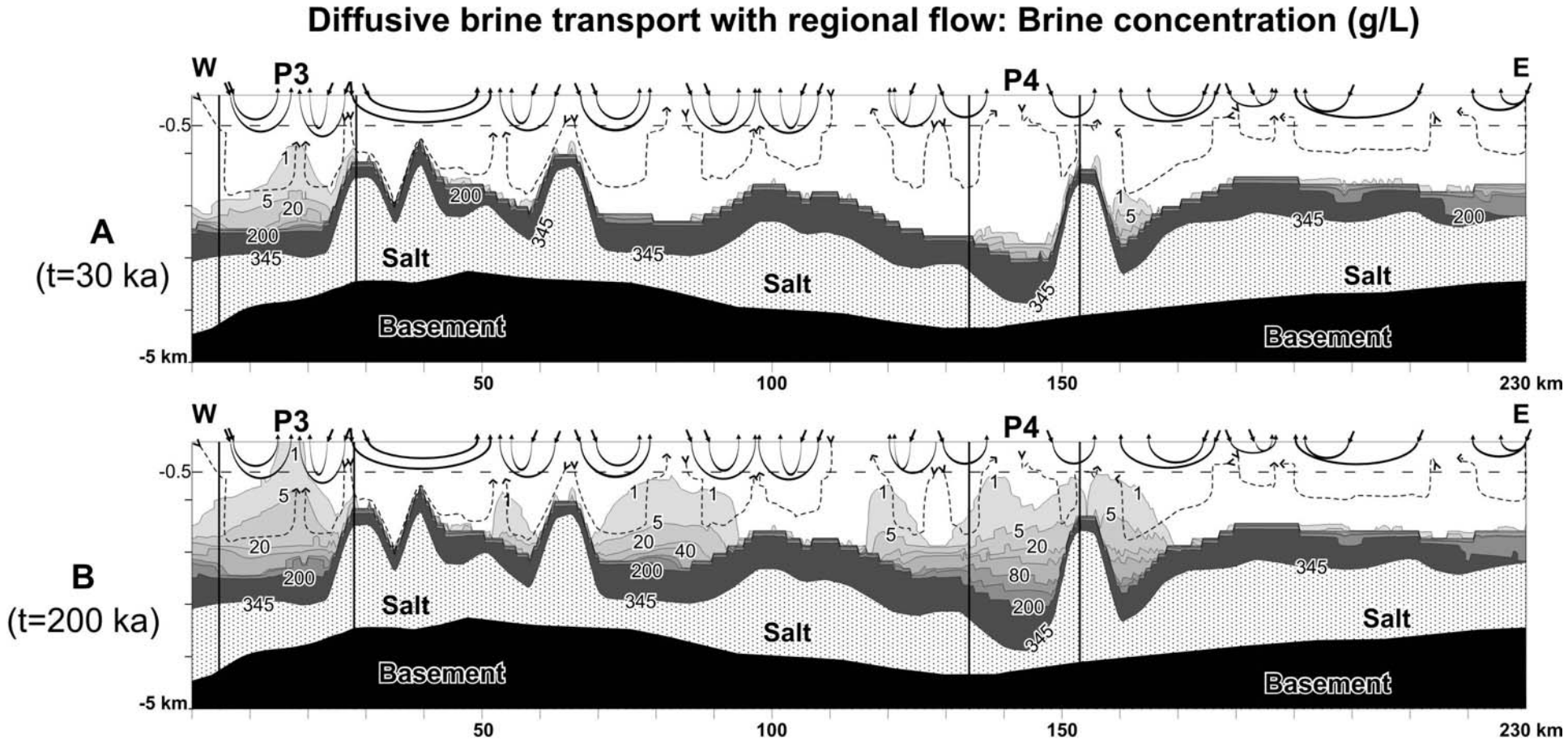

Fig.3-5: A and B: Mass distribution resulting from coupled brine transport and regional flow simulation at $t = 30$ ka and $t = 200$ ka respectively. Salt concentrations are expressed in g/L. Two profiles P3 and P4 are located within the cross-section. The simulation results for these two profiles are shown with no vertical exaggeration in Fig.3.6 and Fig.3.7

In profile P3 (Fig.3-6), the regional flow shows a marked confluence of pore water vectors 9 km from the eastern end of the section at the 19th km mark (Fig.3-6.A1). The peak pore water velocity is 0.7 m yr^{-1} which is a very high value with regard to the range of the velocity flow field in the shallow aquifer (i.e. 0.1 to 0.4 m yr^{-1}). Consequently, in the deeper part of the basin groundwater flows at higher velocities in relation to this intense regional flow. At 2 km depth, groundwater ascends in the upper aquifer at velocities of about 3-5 cm yr^{-1}. As a result, the dissolved halite is advected upward within the basin and salt upconing begins at an early simulation stage ($t = 30$ ka , Fig.3-6.A2). Additionally, upward halite migration is enhanced farther east by the confluent regional flow. On the other hand, downward flow of brine occurs along the salt flank at approximately 1.5 cmyr^{-1} as already discussed in the previous paragraph. At the end of the simulation run, pore water velocities decrease slightly in the deeper part of the basin and along the salt flank since more dissolved halite has filled the sediments (Fig.3-6 B1). At $t = 200$ ka , salty water reaches the surface (Fig.3-6.B2) and leaches through the upper boundary 10 km away from the salt diapir crest in the W-E direction.

By contrast, profile P4 (Fig.3-7.A) shows lower velocities with a uniform flow direction along the entire profile. At 2 km depth the pore water velocity is only 1.5 cm yr^{-1}. Therefore at the beginning of the process salt upconing does not occur ($t = 30$ ka , compare Fig.3-6.A2 with Fig.3-5.A2). A larger period is needed to observe increased concentration gradients within the sediment fill. At $t = 200$ ka (Fig.3-7.B2) brackish water with 1g/L of dissolved salt is found at a depth of 0.5 kilometer in the eastern part of the profile above the salt diapir crest.

In summary, the simulations have emphasized the importance of topography induced fluid flow in affecting salt transport within the basin. Upward or downward migration of dissolved halite is respectively found in relation to ascending or descending fluid circulation due to the regional flow. Salt water upconing occurs only when the regional flow is included in the simulations (compare Fig.3-5 with Fig.3-1).Groundwater flow discharging at high rates in salt diapir environments, where shallow halite dissolution takes place, can possibly lead to surface occurrence of salty water in the lowlands. Herbert et al. (1988) demonstrated that overturn of groundwater above a salt column can result from viscous drag induced by a shallow regional flow.

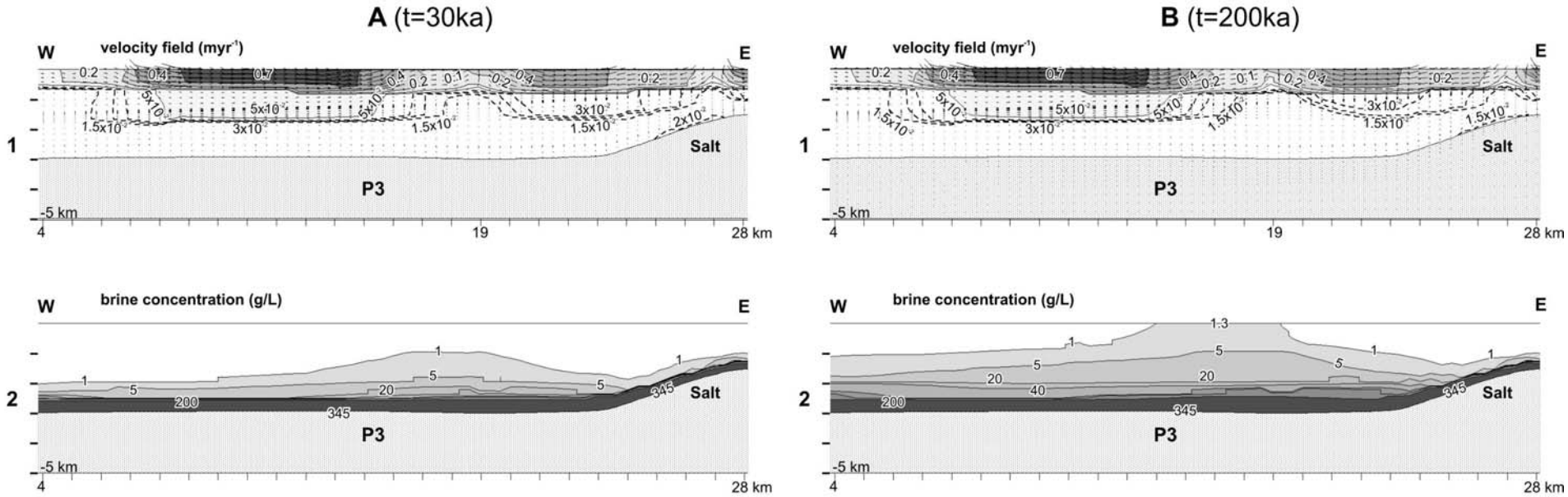

Fig.3-6: A and B: Zoom of the coupled brine transport and regional flow simulation results for profile P3 as located in Fig.3.4 at $t = 30$ ka and $t = 200$ ka respectively . No vertical exaggeration is used. **1:** Pore water velocity field in myr^{-1}. Pore vector linearly scaled to the largest flow arrow. **2:** salt concentrations in g/L

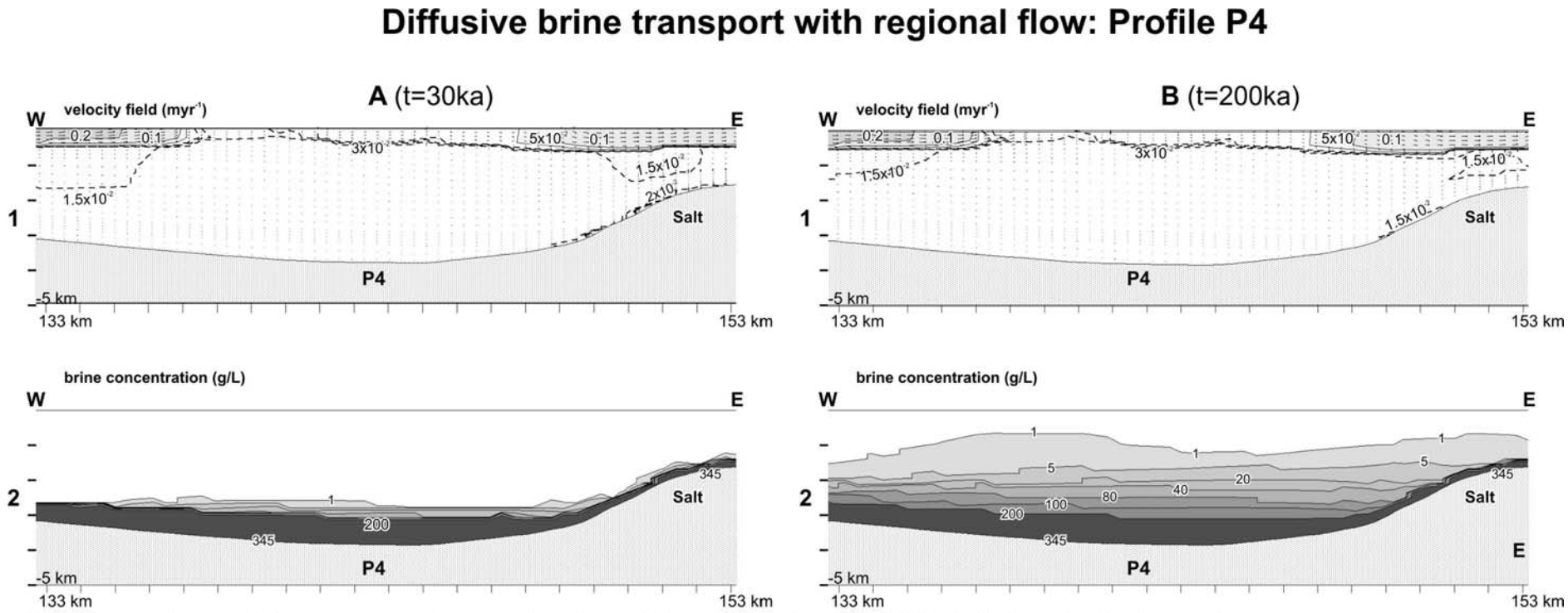

Fig.3-7: Zoom of the coupled brine transport and regional flow simulation results for profile P4 as located in Fig.3.4 at $t = 30$ ka and $t = 200$ ka respectively. No vertical exaggeration is used. **1:** Pore water velocity field in myr^{-1}. Pore vector linearly scaled to the largest flow arrow. **2:** salt concentrations in g/L.

3.2 Thermohaline convection

Thermohaline convective flows are driven by buoyant forces induced by temperature and concentration gradients. In this case, a criterion to predict the onset of instabilities is based on the Rayleigh theory. The key dimensionless number is the Rayleigh number (Ra), which is the ratio between buoyancy-driven forces and resisting forces caused by diffusion and dispersion. For sufficiently high values of Ra greater than some critical Ra_c instabilities will occur in the form of fingers or plumes. This critical Rayleigh number defines the transition between dispersive/diffusive solute transport ($Ra < Ra_c$) and convective transport by density-driven fingers ($Ra > Ra_c$). The Rayleigh stability criterion is discussed in more detail in Appendix 4.

While Rayleigh theory can be successfully used for the study of convective flow in homogenous systems (e.g. at laboratory scale) its applicability for transport processes within geothermal system is seriously questioned (Simmons et al. 2001). This criterion assumes that a steady-state flow takes place in an homogeneous system. Furthermore stability analyses based on dimensionless numbers involve the definition of a characteristic length scale of the porous media through which the temperature and solute gradients are supposed to vary linearly. In all transport processes occurring within real basin systems, such as the NEGB, these conditions are not satisfied. The physical parameters of the basin are subject to large heterogeneities. The brine density model described in paragraph 1.2.3 displays an unstable density profile in which concentration gradients are not linear. The thicknesses of the stratigraphic units of the NEGB can vary from a few meters to some kilometers because of the strong salt tectonics. Therefore, the definition of a representative length scale is rather problematic. Moreover, owing to the steady-state flow assumption made in Rayleigh's theory, the critical number Ra_c cannot provide information about the temporal evolution of the convective flow regime. From these considerations, it follows that the Rayleigh criteria is not convenient (if not impossible) for analyzing density-driven flow within the NEGB. Therefore instead of this dimensionless approach, the fully dimensional equations are used (Eq.(2.1), to Eq.(2.6)).

Thermohaline convection can be either (Oldenburg and Pruess 1998): (1) fingered, where narrow, finger-shaped plumes protrude upwards and/or downwards within the system; (2) penetrative, where convection cells penetrate upwards from the bottom of the system to the

top; (3) layered where convection occurs in stacked convective cells. When there is no convection the system is termed static or conductive.

Since in the NEGB temperature and salinity increase with depth, the destabilizing potential comes from the temperature gradient while the concentration gradient is stabilizing. This regime, also referred to as (double-)diffusive, favors oscillatory instabilities (Nield 1968). Simulation results show that the NEGB system is static in the Buntsandstein and fingered convection occurs in the overburden.

3.2.1 Boundary conditions

The boundary conditions defined for the thermohaline problem are the followings:

- The surface is open to solute and heat outflow. The head boundary condition is either set to a constant value of 25 m in the free convection problem, so that the regional flow is effectively removed from the model, (paragraph 3.2.2) or to the topographic level, used for in the mixed convection (in the paragraph 3.3.3).
- At Top Salt a fixed concentration value of 345.2 g/L has been set.
- At the basement a constant temperature boundary condition is defined. The value is set to 150 °C which corresponds to a linear vertical gradient of 30 °C/km.
- The lateral boundaries are closed to fluid, heat and mass flow

The boundary condition for brine concentration at the surface allows solute outflow through a thin stratum in contact with the top surface of the domain, as defined in paragraph 3.1.1. Since in thermohaline convection solute and thermal effects are strongly coupled, an open boundary condition, allowing heat outflow trough the domain surface, is defined in analogy to mass outflow:

$$\mathbf{q}_{\mathrm{T}}(t) = -\Phi_{\mathrm{T}}(T^{*} - T)\mathbf{n}\,, \tag{3.4}$$

where $\mathbf{q}_{\mathrm{T}}$ is the heat flux, Φ_{T} is a heat transfer coefficient, T^{*} is the prescribed boundary condition value for the temperature T at the surface, and $\mathbf{n}$ is the vector normal to the surface of the domain. If $\Phi_{\mathrm{T}} = 0$ the boundary is adiabatic while when $\Phi_{\mathrm{T}} \to \infty$, $T \to T^{*}$ and therefore the Cauchy boundary condition is reduced to a Dirichlet-type. As for the mass transfer coefficient (Eq.(3.3)), the heat transfer coefficient Φ_{T} can be estimated by rewriting Eq.(3.4) in a Fourier form, viz.:

$$q_T(t) \approx -\lambda_{tr} \frac{T^* - T}{d} \tag{3.5}$$

where d is the thickness of the heat transition layer. The heat transfer coefficient becomes:

$$\Phi_T \approx \frac{\lambda_{tr}}{d} \quad \text{in} \quad \left[Jm^2 s^{-1} K^{-1} \right] \tag{3.6}$$

where λ_{tr} represents a heat conduction coefficient of a thin transition stratum. λ_{tr} can be considered more or less equal to the thermal conductivity of the bordering stratigraphic unit (i.e. Cenozoic, $\lambda_{tr} \approx 1.5\ Jms^{-1}K^{-1}$, Table 1.1). Assuming that surface heat and mass transfer occurs in the same thin stratum in contact with the top surface, $d \sim 1$ m. Hence from Eq.(3.6) $\lambda \approx 1.5\ Jm^2 s^{-1} K^{-1}$. The prescribed surface boundary condition T^* has been set equal to the reference temperature value at the surface, i.e. $T^* = 8$ °C.

3.2.2 Free convection

In this paragraph the results of free convection simulations are presented, in order to investigate the dynamics of thermohaline convection within the NEGB in the absence of regional flow. The numerical results will emphasize the importance of temperature gradients in driving saline water to the surface. Although concentration and temperature distribution are depicted separately, it is worth recalling that in thermohaline convective flow mass and heat transport are strongly coupled and therefore these processes must not be seen as independent.

Fig.3-8 shows the brine concentration at a computing time of 30 ka (A) and at 200 ka (B). While in the Buntsandstein the concentration profile varies linearly from 200 g/L to 345 g/L, as previously, in salt diapir environments brine plumes develop rapidly and penetrate the overburden (Fig.3-8A). Compared to the other part of the profile, a strong brine fingering affects the eastern end of the cross-section. This behaviour is particularly pronounced at the western part of the basin where narrow salty plumes with 1 g/L of dissolved halite are close to or reach the surface. At the end of the simulation (Fig.3-8B), the mass pattern above the Buntsandstein displays two different features:

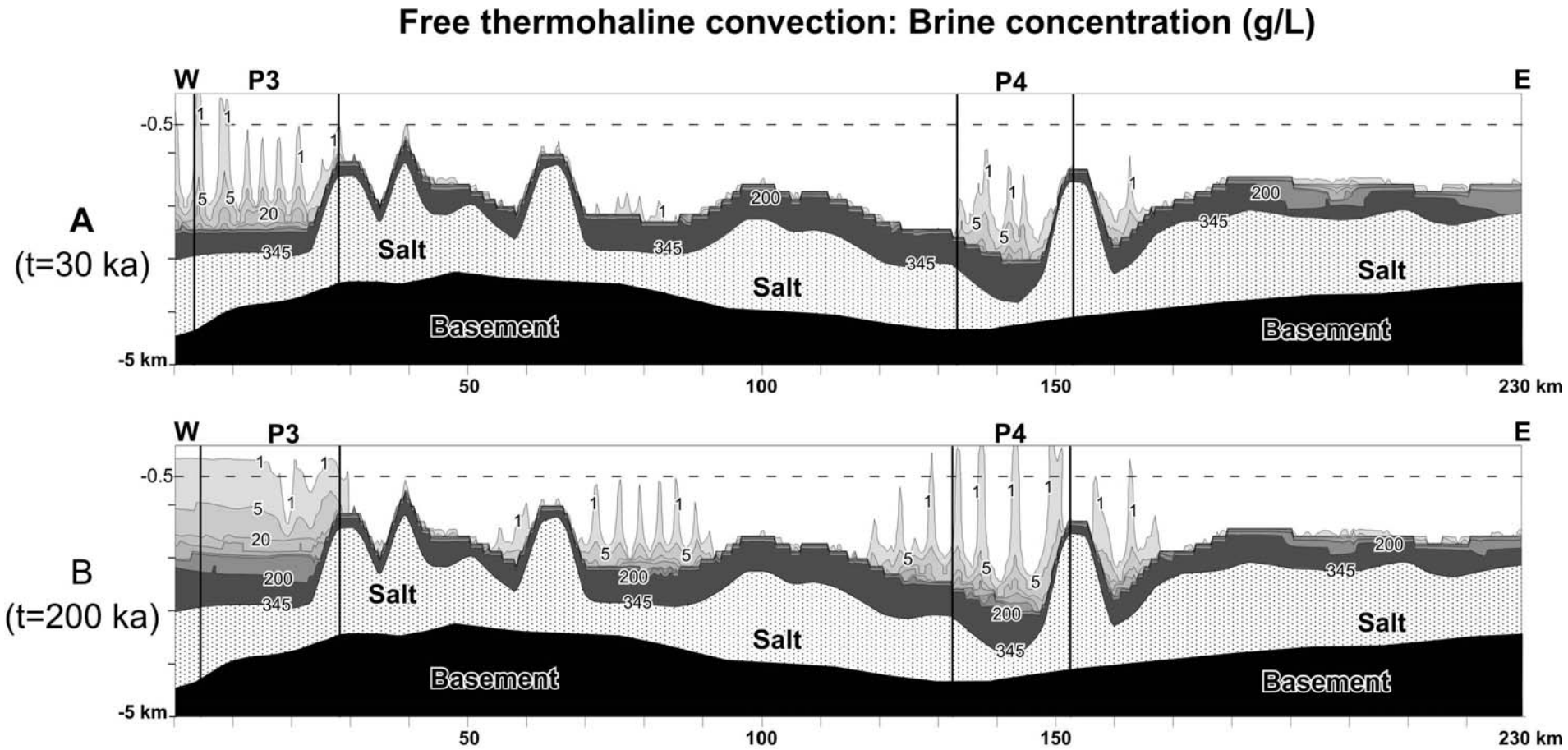

Fig.3-8: A and B: Mass distribution resulting from free thermohaline simulation at $t = 30$ ka and $t = 200$ ka respectively. Salt concentrations are expressed in g/L. Two profiles P3 and P4 are located within the cross-section. The simulation results for these two profiles are shown with no vertical exaggeration in Fig.3-10 and Fig.3-11

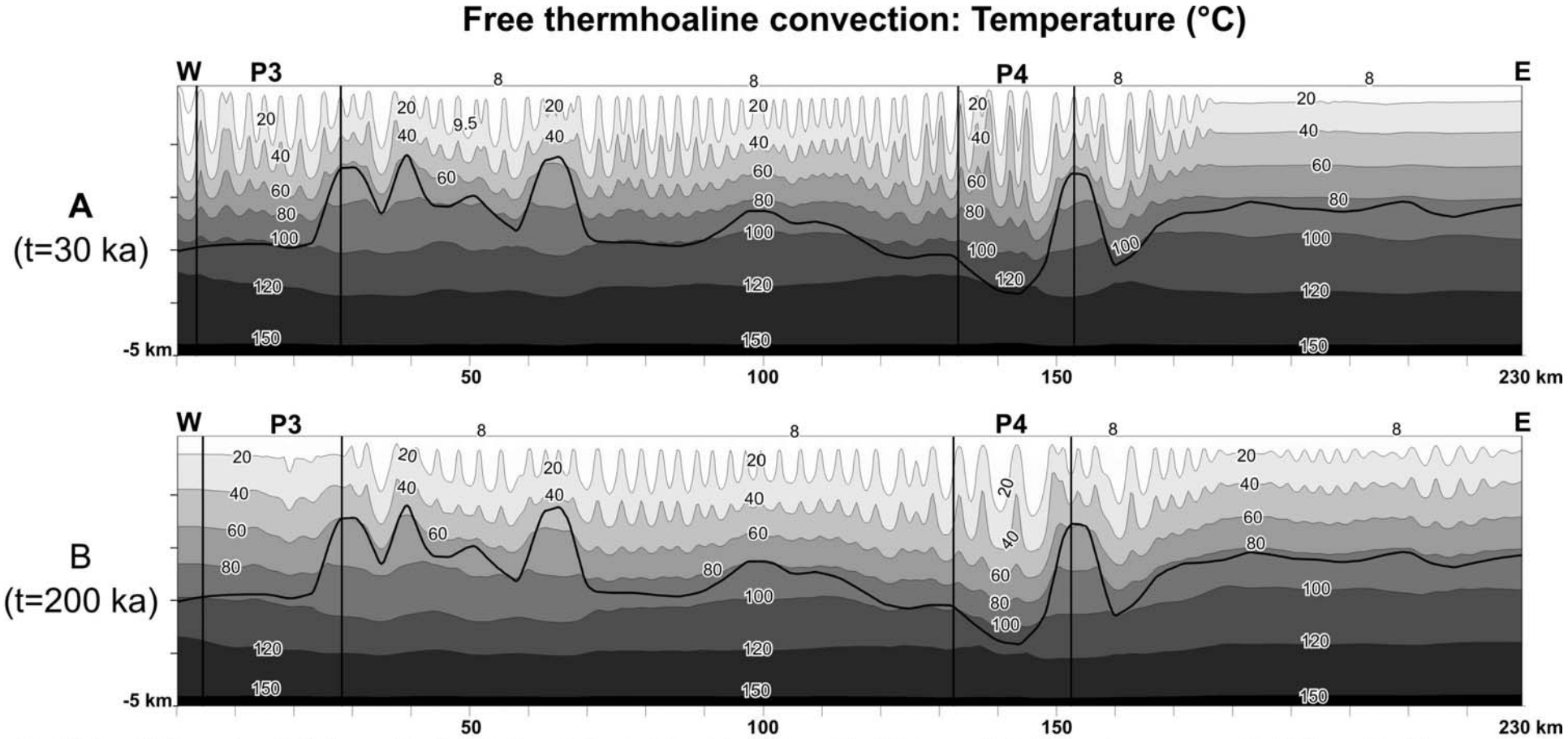

Fig.3-9: A and B: Temperature distribution resulting from free thermohaline simulation at $t = 30$ ka and $t = 200$ ka respectively. Temperatures are expressed in °C. Two profiles P3 and P4 are located within the cross-section. The simulation results for these two profiles are shown with no vertical exaggeration in Fig.3-10 and Fig.3-11

- At the western part of the basin, the finger regime disappears at the end of the simulation. Instead, the concentration isopleths are flat and the salt content increases almost linearly with depth. However, in the neighbourhood of the salt dome, a depressed concentration gradient is displayed. The layered brine stratification is likely a boundary effect. Since the lateral boundaries of the model are closed to fluid flow, mass and heat transfer, the dissolved halite cannot diffuse away in the western direction. Moreover, salt diffusion in the eastern direction is also prevented due to the presence of shallow salt diapirs. Therefore, as time progresses, the sediments are filled with halite. The finger regime evolves into a layered system in which concentration increases with depth.
- Within the rest of the basin, the fingers have kept on protruding even after 200 ka. The salty plumes have reached half a kilometre depth in the central part of the basin. At the 150^{th} km mark near the salt diapir, slender brackish fingers extend over 3 km throughout the sediments up to the surface. On the other hand, at the eastern part of the basin, far from the salt dome, no salty plumes develop.

The temperature field (Fig.3-9) displays a disturbed profile throughout the sediment fill above the Zechstein unit. These oscillatory patterns are characteristic of a multicellular convective regime and already occur at early time stages (Fig.3-9 A, $t = 30$ ka). The waves are non-periodic and their amplitude decreases with depth. At the eastern part of the basin, far from the salt diapir the temperature distribution is not less disturbed. The temperature gradient did not diverge from the initial conditions and increases linearly with depth. Below the Zechstein unit the temperature profile is everywhere conductive showing the well-known thermal anomalies within the salt diapirs (i.e. concave temperature isopleths). At $t = 200$ ka (Fig.3-9 B), the temperature profile still displays convective oscillations above the Zechstein. However, at the western part of the basin, the temperature isopleths are nearly flat presenting only one anomaly near the salt dome. Minor temperature oscillations have developed at the eastern part of the basin. On the other hand, the conductive regime dominates in the sediments below the Zechstein unit.

Fig 3.8 and 3.9 provided a regional picture of mass and temperature distribution within the whole cross section. The calculated patterns show both features of thermohaline and static regime: brine fingers penetrate in the sediments above the Buntsandstein unit, the thermal anomalies are manifested as non-periodic waves which intensity decreases with depth. As time progresses, a layered stratification of the brine concentration is achieved at the western part of the basin. On the other hand, the concentration profile within the Buntsandstein unit is steady and increases linearly up to the saturation value (345 g/L) at top salt. Therein the temperature profile is slightly disturbed and becomes conductive below the Zechstein unit.

In order to gain insights into the geometry of the convective cells and to quantify their effects on the mass and temperature field, the simulation results are illustrated with no vertical exaggeration for two profiles (denoted with “P3” and “P4” in Fig.3-8 and Fig.3-9) in Fig.3-10 and Fig.3-11 respectively. Early in the simulation process, the profile P3 is affected by a sequence of convective cells in the west-east direction (Fig.3-10 A). The cells extend from a depth of 2 km up to the surface. The cells geometry displays broad areas of recharge (2-3 km wide) with downward directed flow and narrow discharge areas (500 m) up to the surface. The pore water velocities range from 1.5 cm yr^{-1} at the bottom of the cell to 0.3 m yr^{-1}at the surface. Along the salt edge of the diapir, groundwater flows downward at 1.5 cm yr^{-1}. Throughout the profile, salty fingers develop in relation to upward convective flow (Fig.3-10 A2). At the western part of the basin, a salty plume reaches the surface. At that location, brine with 1.2 g/L of dissolved halite leaches throughout the surface at 0.3 m yr^{-1}. Within the Buntsandstein the concentration gradient is linear due to salt diffusion. The temperature field (Fig.3-10 A3) presents oscillatory thermal anomalies down to 2 km of depth because of the convective regime. The amplitude of the waves decreases with increasing depth. Below the Top Zechstein, the heat regime is conductive, presenting flat isopleths. Owing to the natural boundary condition at the surface, temperature values higher than the reference surface value (i.e. 8°C) occur in association with increased temperature gradients. The temperature values at the surface span between 8°C and 9.6°C. A straightforward relation between the thermally induced convective cells, the mass and the temperature fields is inferred by comparing Fig.3-10 A1 with Fig.3-10 A2 and A3. Concentration and temperature distributions show broad areas of fresh and cooler water in the recharge zone while narrow salty and warmer plumes occur in the up-flows. Peak brine concentration and temperature values at the surface are associated with vigorous upward flow induced by thermal convection as it is the case at the western part of the basin.

At the end of the simulation run, the convective regime throughout the profile vanishes (Fig 3.10 B1). The vectors show stagnation zones with very low pore velocities in which a diffusive/conductive regime has been achieved. Only two weak convective cells recharge the sediments in the shallow aquifer at the eastern part of the profile. In relation to these downward freshwater flows, concentration and temperature display a depressed profile (Fig.3-10 B2, B3).

As in Profile 3, Profile 4 reveals an intense convective regime at early time stage (Fig.3-11 A). Here the recharge areas are larger (3-5 km wide) and upward flows discharge to the surface at higher rates (0.3-0.4 myr^{-1}). Thermally induced brine fingers begin to protrude within the sediment fill (Fig.3-11 A2), reaching a depth of approximately 1 km below the

surface. The temperature field presents the same features described previously: a non-periodic convective oscillatory regime affects the profile down to 2 km depth. The amplitudes decrease with depth and a conductive regime is achieved below the Zechstein Salt.

At $t = 200$ ka , the thermohaline finger regime persists (Fig.3-11 B). The pore velocities have drastically decreased (7 cm yr^{-1} to 0.2 m yr^{-1}) as more saline and heavier water has been advected up to the surface (Fig.3-11 B2) by thermal buoyant forces. At the surface, brine concentrations range from 1 to 1.6 g/L. On the other hand, the downward flow forms broad areas of freshwater which shape the trough between the brine fingers. In relation to the narrow brine plumes and the wide freshwater cells, the subsurface temperature gradient is respectively increased or depressed (Fig.3-11 B3). Consequently, the surface temperature is higher than or equal to the reference temperature value (8°C). Peak values of discharge flow, brine concentration and fluid temperature at the surface occur at the eastern part of the profile.

From the numerical simulation, it turns out that saline and thermal plumes rose together spreading over the same areas within the sediment fill. This feature is displayed in Fig 3.10 A and in Fig.3-11 A and B. This phenomenon characterizes the strong coupling of heat and mass transfer in thermohaline convection and is explained by Oldenburg and Pruess (1998;1999): because of the thermal retardation factor (Eq.(1.18), Appendix 1) the concentration front tends to advance ahead of the temperature front; however, the increased salt concentration at the leading edge of the brine plume diminishes upward buoyancy force. Therefore, owing to this lack of positive buoyancy the brine cannot advance beyond the region of increased temperature. The brine and the temperature plume reach the same height occupying the same region. The heat retardation factor induces the formation of a “density lid” at the top of the brine plumes. Oldenburg and Pruess (1998;1999) suggest that the presence of density lids can promote lateral flow of the plume. Accordingly, in Fig.3-11 B2 the brine finger at the eastern part of the profile presents a bifurcated tip spreading laterally at both sides of the plume.

Free thermhoaline convection: Profile P3

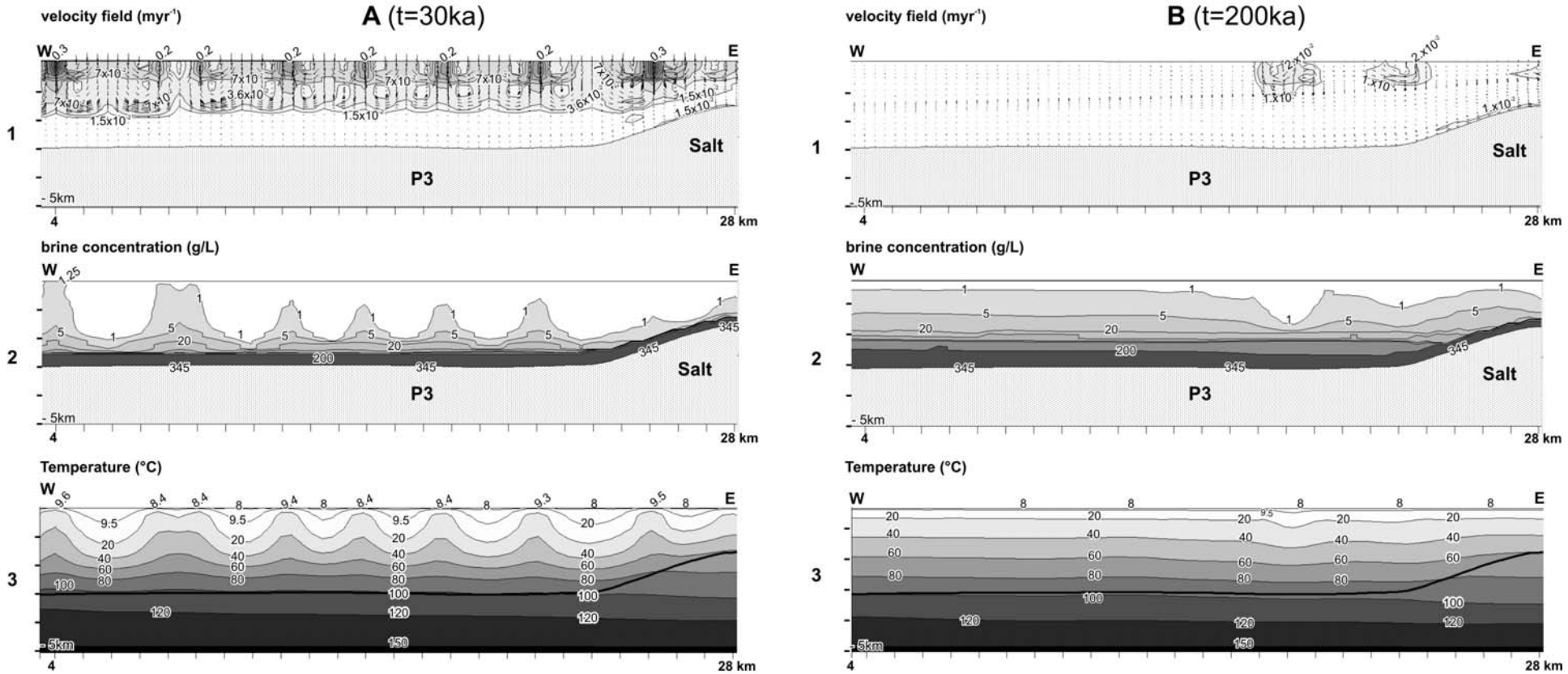

Fig.3-10: A and B: Zoom of the thermohaline simulation results for profile P3 as located in Fig.3-8 at $t = 30$ ka and $t = 200$ ka respectively . No vertical exaggeration is used. **1:** Pore water velocity field in myr^{-1}. Pore vector linearly scaled to the largest flow arrow. **2:** salt concentrations in g/L. **3:** temperature distribution in °C

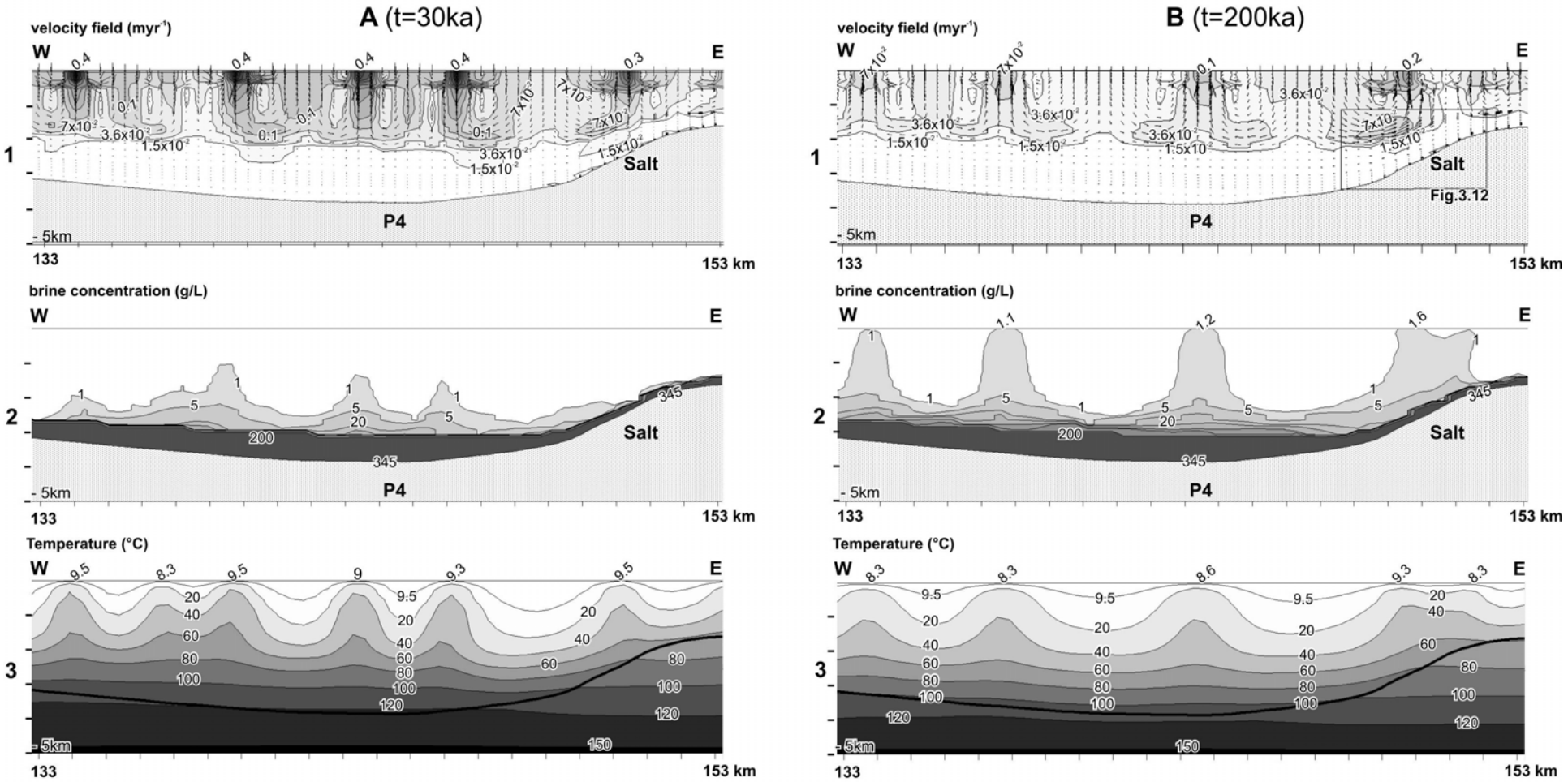

Fig.3-11: A and B: Zoom of the thermohaline simulation results for profile P4 as located in Fig.3-8 at $t = 30$ ka and $t = 200$ ka respectively . No vertical exaggeration is used. **1:** Pore water velocity field in myr^{-1}. Pore vector linearly scaled to the largest flow arrow. **2:** salt concentrations in g/L. **3:** temperature distribution in °C. The rectangle locates a salt diapir flank. Velocity and temperature field within this salt diapir environment are further illustrated in Fig.3-12

An additional feature of thermohaline convection is the presence of an upward flow in the neighbourhood of salt diapirs. A zoom of the calculated pore velocity and temperature fields in a salt dome environment is shown in Fig.3-12. Downward forces resulting from the gravitational field control groundwater flow along salt diapirs flank. The salt-laden water sinks at approximately 1.5 cm yr^{-1} (Fig.3-11 (1)). However an upward flow paralleling this descending flow occurs in the overlying unit at approximately 1 cm yr^{-1}. This phenomenon can be explained by the temperature distribution (Fig.3-12 (2)). Because of the thermal conductivity contrast between salt and overlying sediments the isotherms are convex near the edge of the salt diapir. The increased temperature gradient causes a decrease in fluid density near the salt dome. This drives the groundwater flow toward the salt dome and initiates the uprising circulation of brine within the neighbouring sediments. The thermally induced upward flow counteracts the downward brine motion occurring along the salt edge. As a result, a thin boundary layer displaying zero pore water velocities develops between the two opposed flows. Free thermohaline convection near salt diapirs has been numerically investigated by Evans et al. (1989 ; 1991). In their studies, the authors tested the effects of different thermal conductivity ratio in the sediments overlying a salt diapir and found that elevated isotherms near salt diapirs can generate thermally induced upward brine circulation.

In summary, temperature effects on brine transport are inferred by comparing the results of pure diffusive brine transport (Fig.3-1) and free thermohaline simulations (Fig.3-8). At an early time stage of the pure diffusive regime (Fig.3-1 A) dissolved halite diffuses along the salt domes edges in the deep sediments. On the other hand, in free thermohaline convection (Fig.3-8 A) stretched salty plumes develop in salt dome environments and protrude vertically throughout the overburden. At the end of the simulation run, in the case of pure diffusive brine transport (Fig.3-1 B), the salty plumes are layered, extending laterally from the salt diapirs flanks over 30 km. Brines with 1 g/L of dissolved salt occur at a depth between 1 km and half a kilometre and do not reach the surface whereas the concentration field resulting from thermohaline simulations (Fig.3-8 B) reveals both subsurface brine occurrence and finger patterns leaching through the surface.

Free thermhoaline convection: Salt flank profile

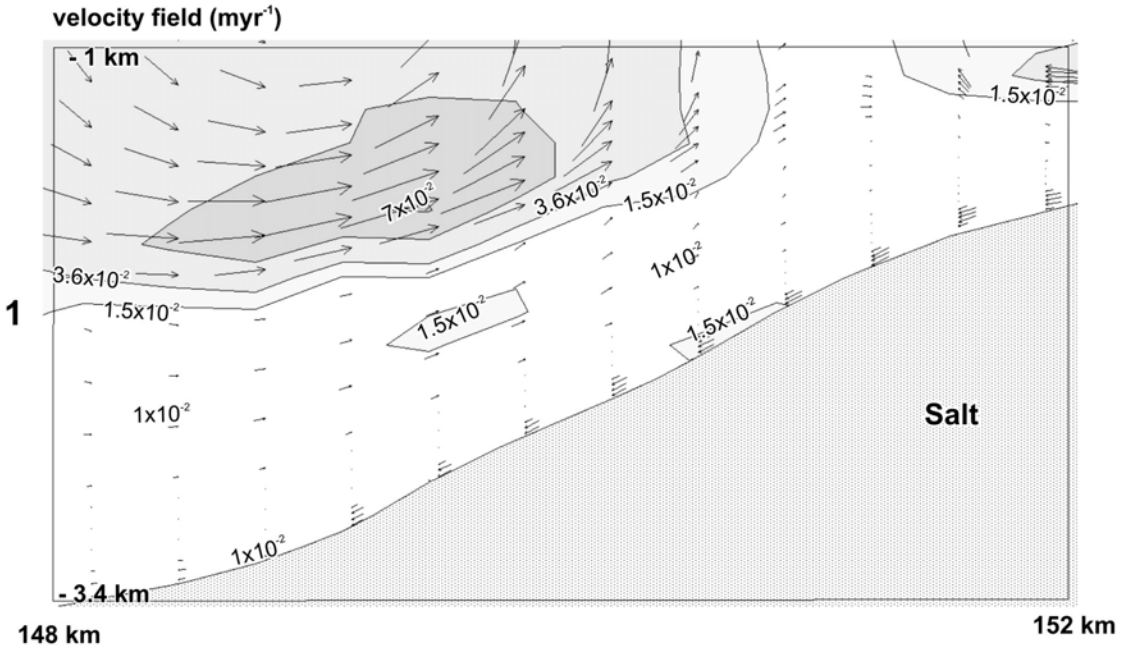

1

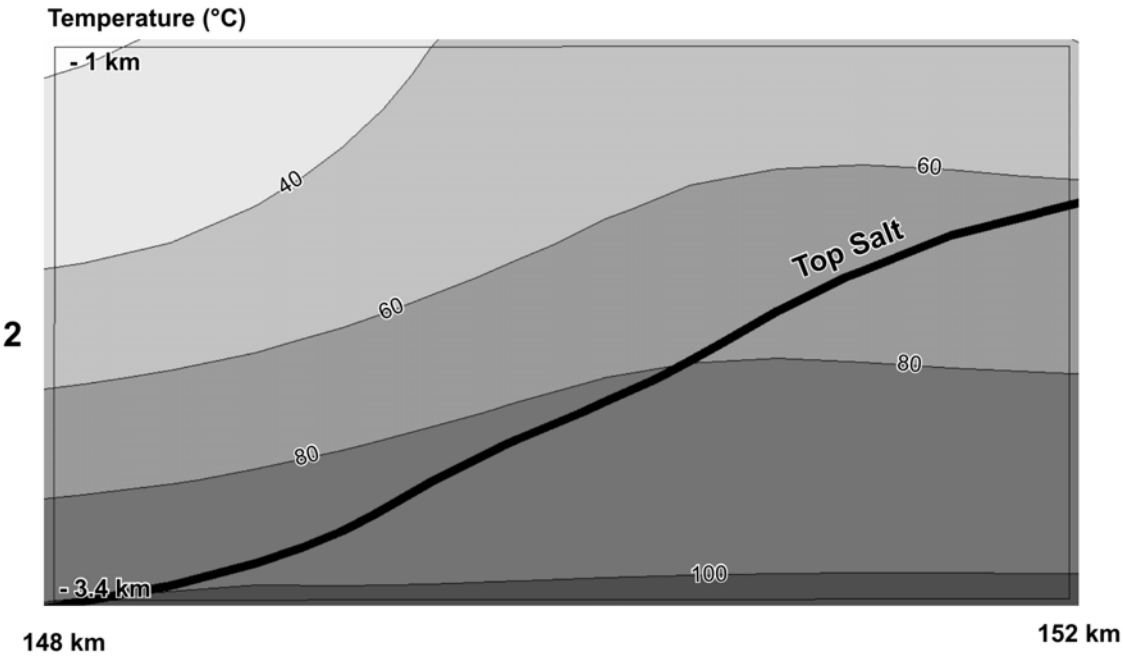

2

Fig.3-12: Zoom of thermohaline simulation results in the salt dome environment as located in Fig.3-11
1: Pore water velocity field in myr^{-1}. Pore vector linearly scaled to the largest flow arrow. **2:** temperature distribution in °C

In diffusive regimes, pore water velocities range between a few millimetres to 1.5 cm per year along salt diapir flanks (Fig.3-2 and Fig.3-3). Thermally buoyant forces instead generate convective cells advecting solute up to the surface at 10-20 cm yr^{-1} (Fig.3-10 and Fig.3-11). Furthermore, the buoyant forces resulting from increased temperature gradients in the sediments overlying the edges of salt diapirs are strong enough to overcome the gravitational field. Consequently upward flow of deep seated salty water occur along salt domes (Fig.3-12),

These features do not occur in the pure diffusive case in which only downward and lateral brine migration can be observed (compare Fig.3-12 with Fig 3.3).

A general aspect of the thermohaline regime is the strong coupling of heat and mass transport which is manifested by salty and thermal plumes rising together and spreading over the same areas (Fig.3-10 and Fig.3-11)

3.2.3 Mixed convection

When an external factor such as head-driven groundwater flow (forced convection) is imposed on a free thermohaline system the resulting regime is referred to as mixed convection. Here the head level is set equal to the topographic relief so that regional and thermally induced flow occur together. In this paragraph, the results from free thermohaline and mixed convection are compared in order to demonstrate the effects of the regional flow on the thermally induced flow.

In Fig.3-13, the brine concentration profile resulting from mixed convection is illustrated together with the simplified regional flowlines. The mass distribution shows significant differences with regard to the profile derived from the free thermohaline simulation (Fig.3-8).

In the mixed convection regime, the thermally induced brine patterns are affected by the regional flow: the narrow salty fingers observed in the free thermohaline regime (Fig.3-8) evolve into a smaller number but larger brine plumes which reach the surface at the discharge areas (Fig.3-13). On the other hand, the brine patterns display a truncated profile in direct relation to the downward flow of freshwater.

The regional flow strongly influences heat transport as well. The short wavelengths of the temperature oscillations characterizing the free thermohaline regime (Fig.3-9) are not preserved in the mixed convection system (Fig.3-14). The isotherms are shaped by the regional flow: in the recharge areas, the infiltration of cooler water depresses the temperature gradient whereas uprising of hot plumes occur in relation to the discharge areas.

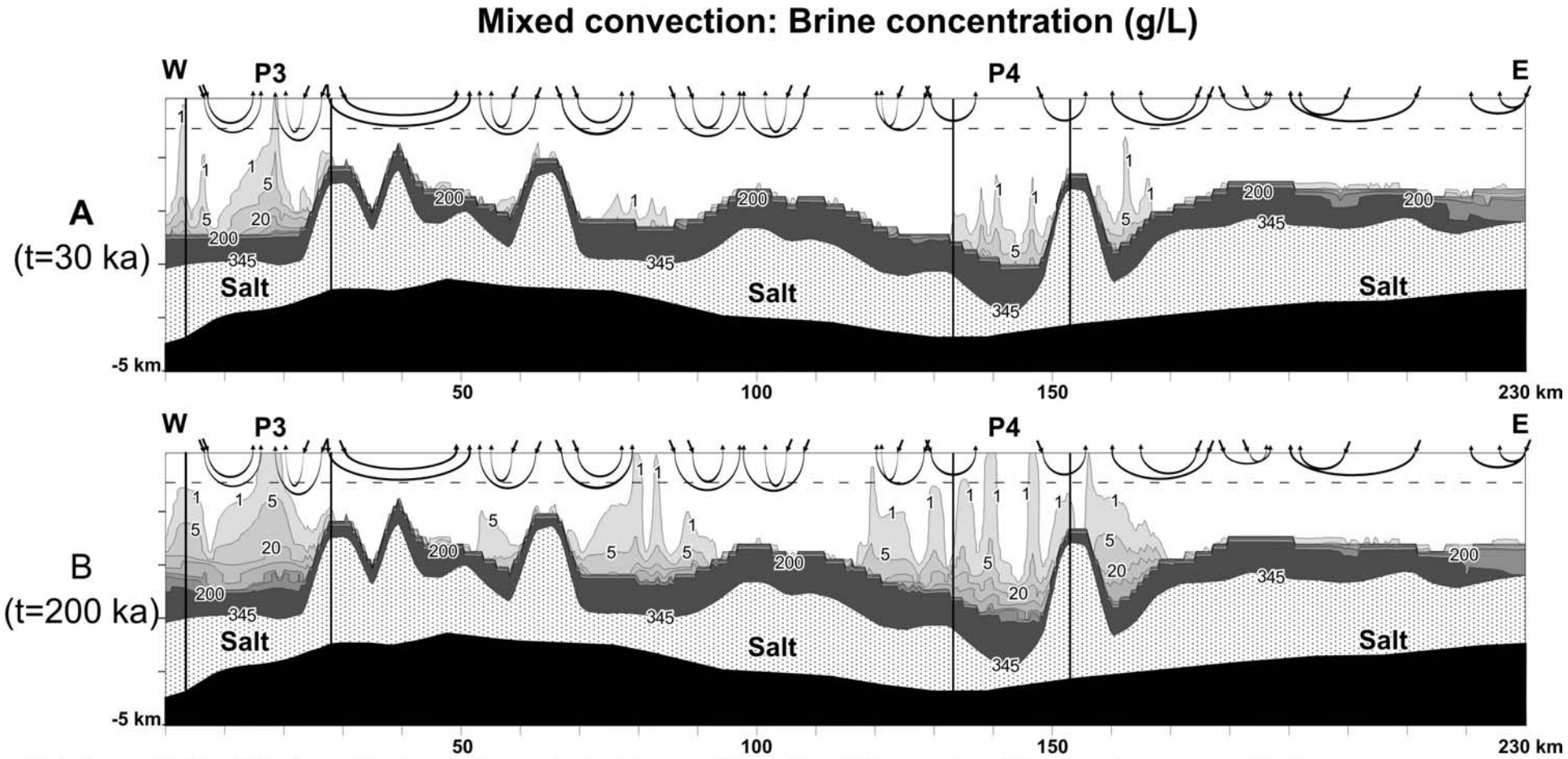

Fig.3-13: A and B: Mass distribution resulting from mixed convection simulation at $t = 30$ ka and $t = 200$ ka respectively. Salt concentrations are expressed in g/L. Two profiles P3 and P4 are located within the cross-section. The simulation results for these two profiles are shown with no vertical exaggeration in Fig.3-15and Fig.3-16

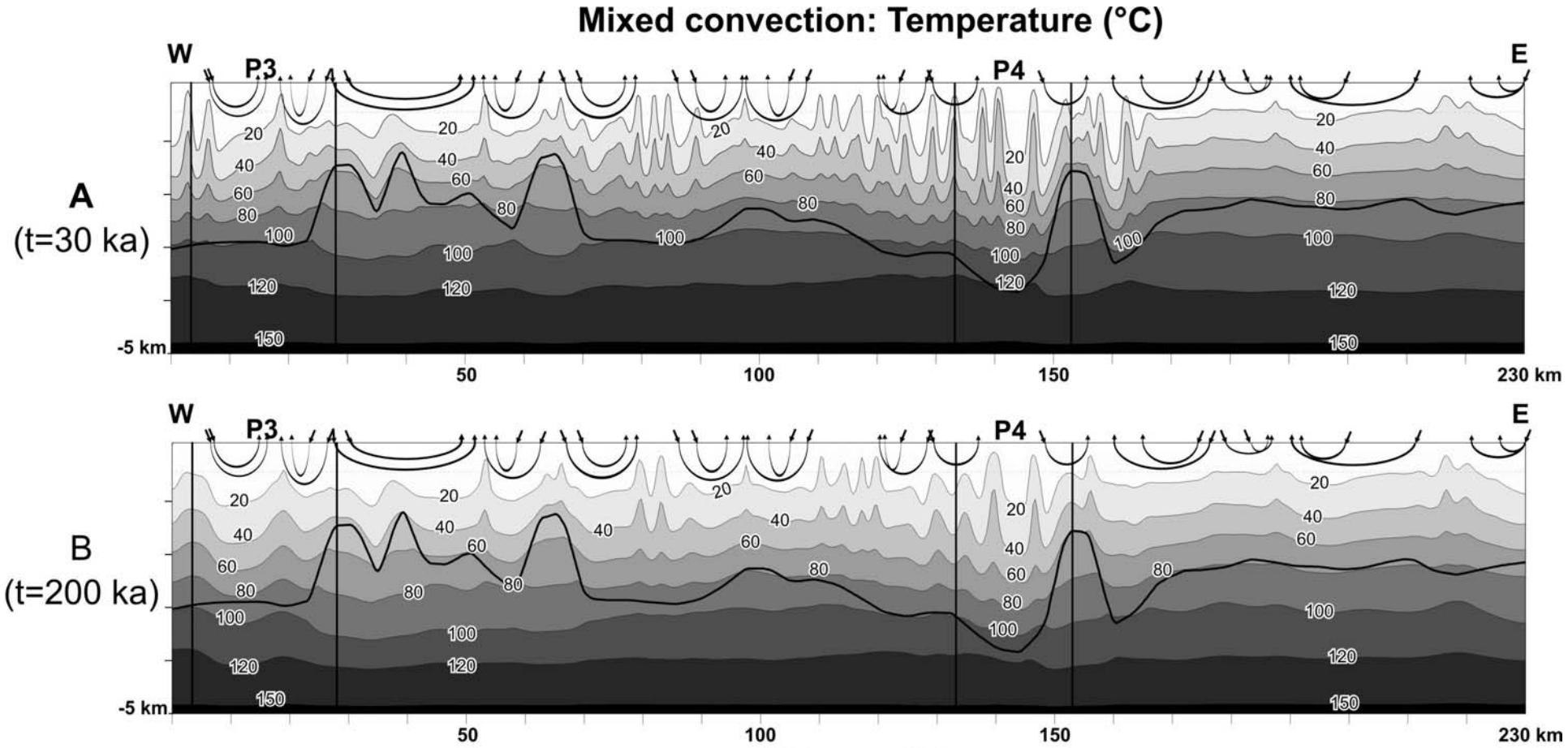

Fig.3-14: A and B: Temperature distribution resulting from mixed convection simulation at $t = 30$ ka and $t = 200$ ka respectively. Temperatures are expressed in °C. Two profiles P3 and P4 are located within the cross-section. The simulation results for these two profiles are shown with no vertical exaggeration in Fig.3-15 and Fig.3-16

Additional insights into these general features of the mixed convection regime are derived from the time dependent analysis of velocity, brine and temperature fields. The two profiles "P3" and "P4" are illustrated without vertical exaggeration in Fig.3-15 and Fig.3-16 respectively at two computing time steps (A: $t = 30$ ka , B: $t = 200$ ka).

At the begin of the simulation process, the velocity field P3 (Fig.3-15 A1) displays thermally induced convective cells only at the western end of the section below the shallow regional flow. Elsewhere, the convective cells which affect the profile in the free thermohaline regime (Fig.3-10 A1) are overwhelmed by the more vigorous regional flow. In relation to the persisting convective regime, a thermally induced brine plume begins to form at the western end of the profile (Fig.3-15 A2 B2). On the other hand, in the central part of the basin, both saline and thermal plumes are advected by the strong regional flow toward the discharge area. As time progresses, the western convective cells vanish (Fig.3-15 B1). Throughout the whole profile, solute and temperature isopleths are dragged parallel to the regional streamlines (Fig.3-15 B2 B3) and brine with 2 g/L spreads over the area of flow confluence.

In profile P4 (Fig.3-16) topography induced flow occurs at the eastern and western end of the profile at 0.1 m yr^{-1}. This relatively small flow rates play a minor role at early time steps (Fig.3-16 A). The thermohaline cellular patterns develop through the whole profile as in the free thermohaline regime (Fig.3-11 A), however with a slightly different spatial distribution. At the end of the simulation run (Fig.3-16 B1), the thermally induced cells weaken since more heavy brine has been advected upward. Therefore the convective cells are swallowed up by the overlying stronger regional flow. Consequently, the growth of brine and thermal plumes is inhibited by the horizontal freshwater flow (Fig.3-16 B2). The resulting patterns display flat fronts adjacent to the regional streamlines. By contrast, finger plumes continue protruding up to the surface in the central part of the profile where the regional flow is almost absent. Therein, solute and thermal fingers spread over the same area within the sediments fill (Fig.3-16 B2 B3), as in the free thermohaline regime.

The numerical results show that in mixed convection, head-driven flow plays an important role in controlling both brine and heat transport. When the regional flow is stronger than thermally induced flow, the hot brine is advected toward the discharge area. As a result, the plumes are shaped by regional flow patterns. On the other hand, in the areas of the basin where the regional flow rates are smaller than the thermally induced velocities, brine and thermal fingers self-develop as in a free thermohaline regime.

Mixed convection: Profile P3

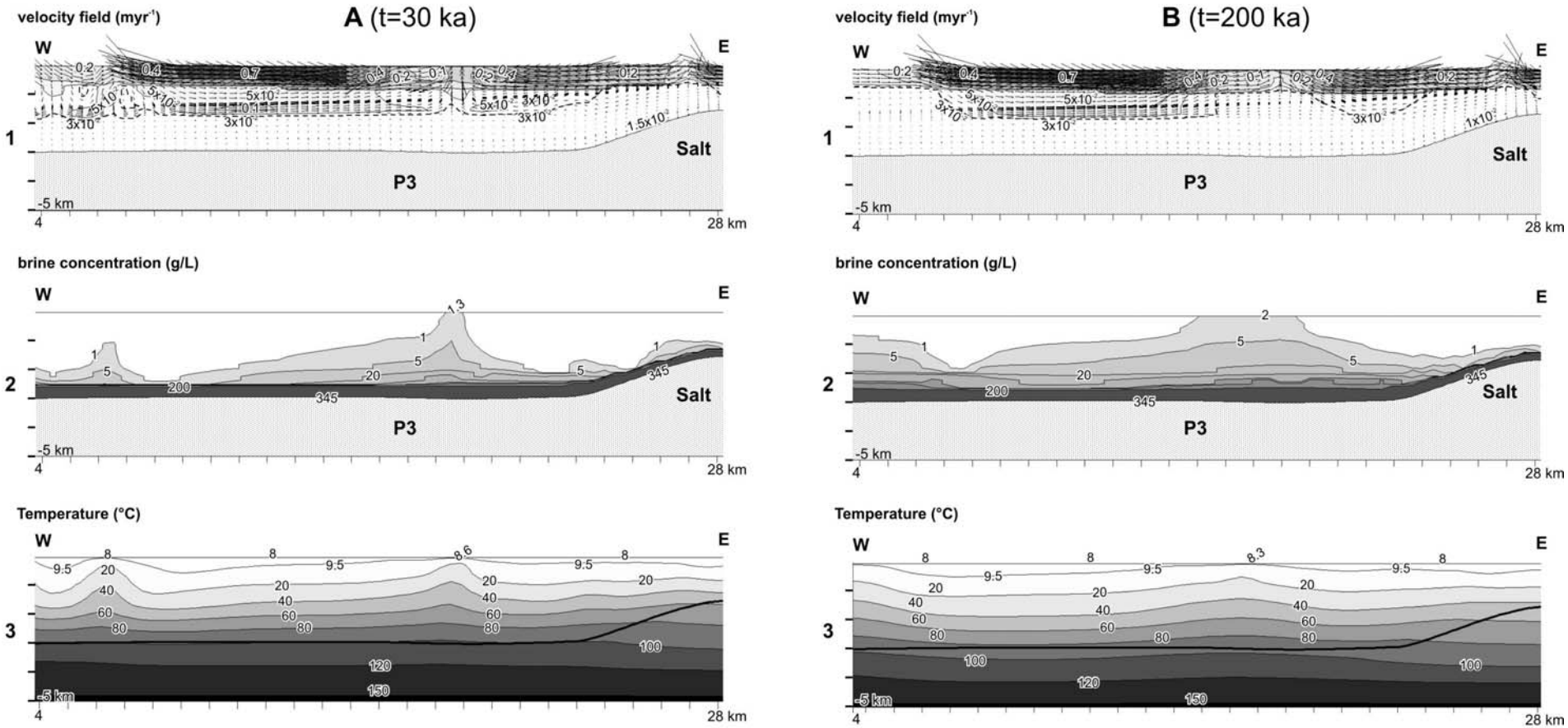

Fig.3-15: A and B: Zoom of the mixed convection results for profile P3 as located in Fig.3-12 at $t = 30$ ka and $t = 200$ ka respectively . No vertical exaggeration is used. **1:** Pore water velocity field in myr^{-1}. Pore vector linearly scaled to the largest flow arrow. **2:** salt concentrations in g/L. **3:** temperature distribution in °C

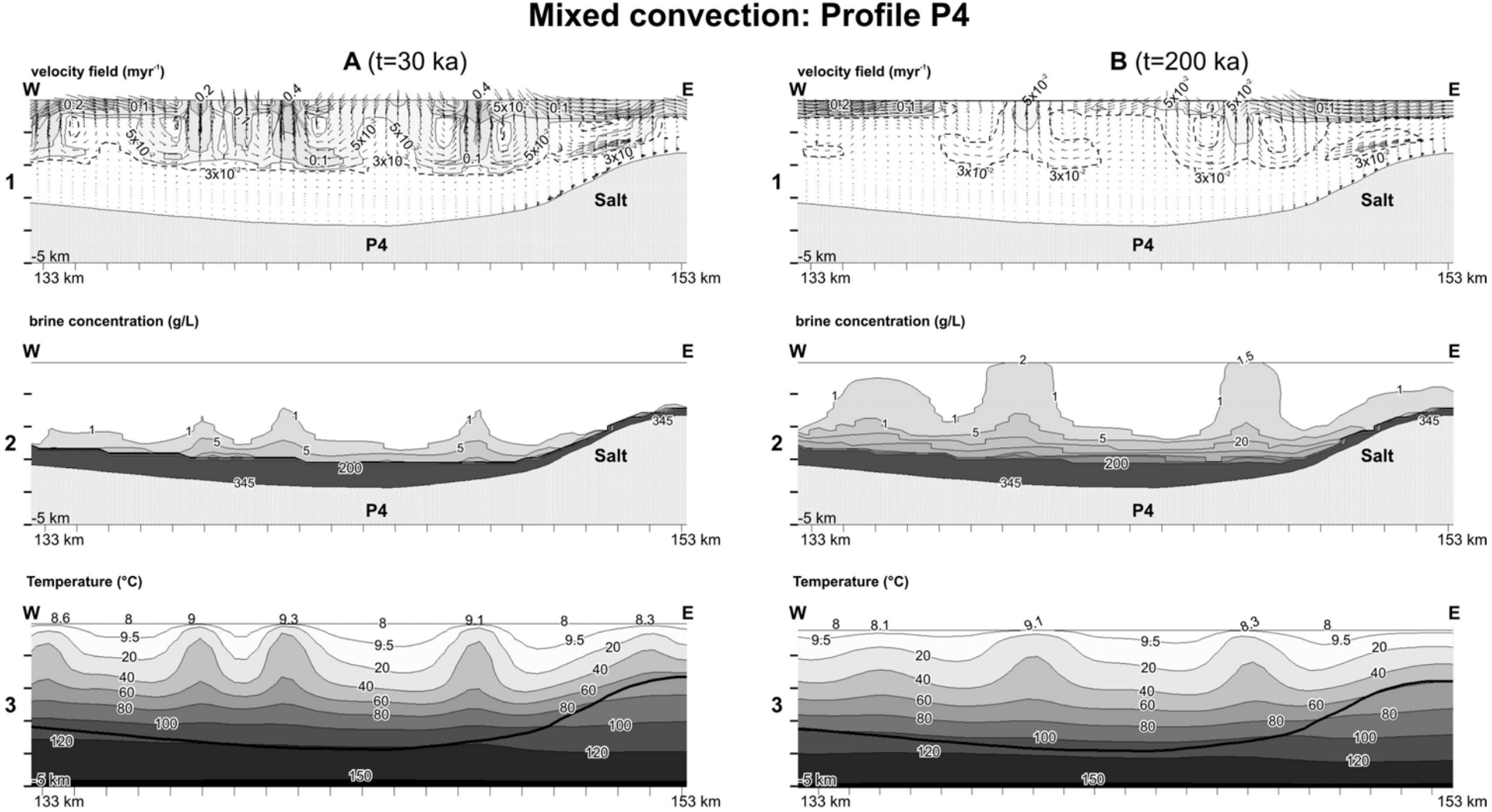

Fig.3-16: A and B: Zoom of the mixed convection results for profile P4 as located in Fig.3-12 at $t = 30$ ka and $t = 200$ ka respectively . No vertical exaggeration is used. **1:** Pore water velocity field in myr^{-1}. Pore vector linearly scaled to the largest flow arrow. **2:** salt concentrations in g/L. **3:** temperature distribution in °C

3.2.4 Viscosity effects

Viscosity is a fluid property which strongly depends on temperature and salinity content. As shown in Fig.3.17, at freshwater condition an increase in temperature from 0 to 350 °C leads to a decrease in viscosity by over 1 order of magnitude.

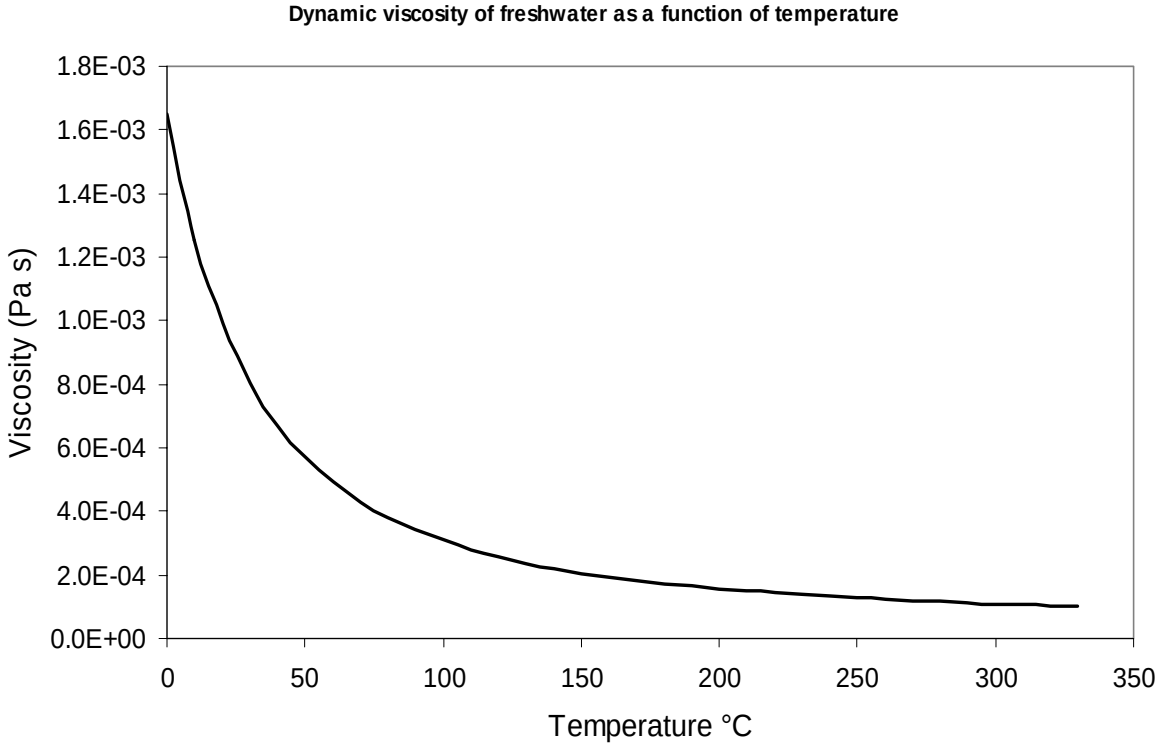

Fig.3.17: Dynamic viscosity of freshwater as a function of temperature.

As seen in Eq.1.10 (Appendix 1), the hydraulic conductivity is inversely proportional to the fluid viscosity. Therefore the intrinsic hydraulic conductivity of the stratigraphic units increases with temperature. This enhances the instability of the layers and promotes thermal convection because of an increase of the Rayleigh number (Eq.4.1 and Eq.4.2, Appendix 4). Consequently, convective flows is more intense than in setting which neglect viscosity.

In this paragraph, viscosity effects on the mixed convective regime are investigated. In FEFLOW® 5 (WASY-GmbH 2002), concentration and temperature dependencies of the fluid viscosity can be included into the model by the use of empirical relationships as given by Lever and Jackson (1985) and by Mercer and Pinder (1974). The resulting brine patterns are illustrated in Fig.3.18 at two time steps (A: $t = 30$ ka and B: $t = 30$ ka).

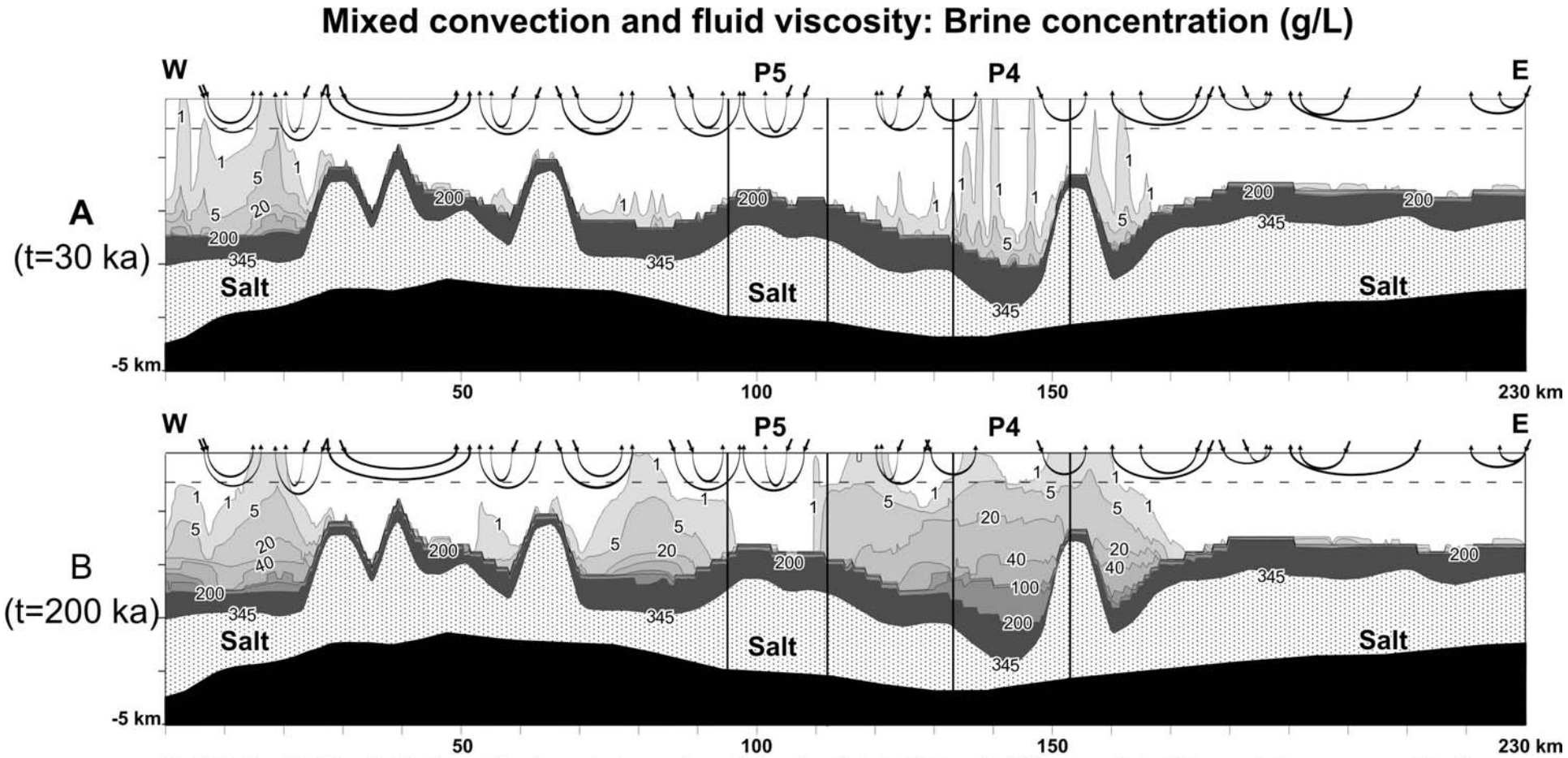

Fig-3.18: A and B: Mass distribution resulting from mixed convection and viscosity effects at t=30 ka and t=200 ka respectively. Salt concentrations are expressed in g/L. Two profiles P4 and P5 are located within the cross-section. The simulation results for these two profiles are shown with no vertical exaggeration in Fig.3.20 and Fig.3.21

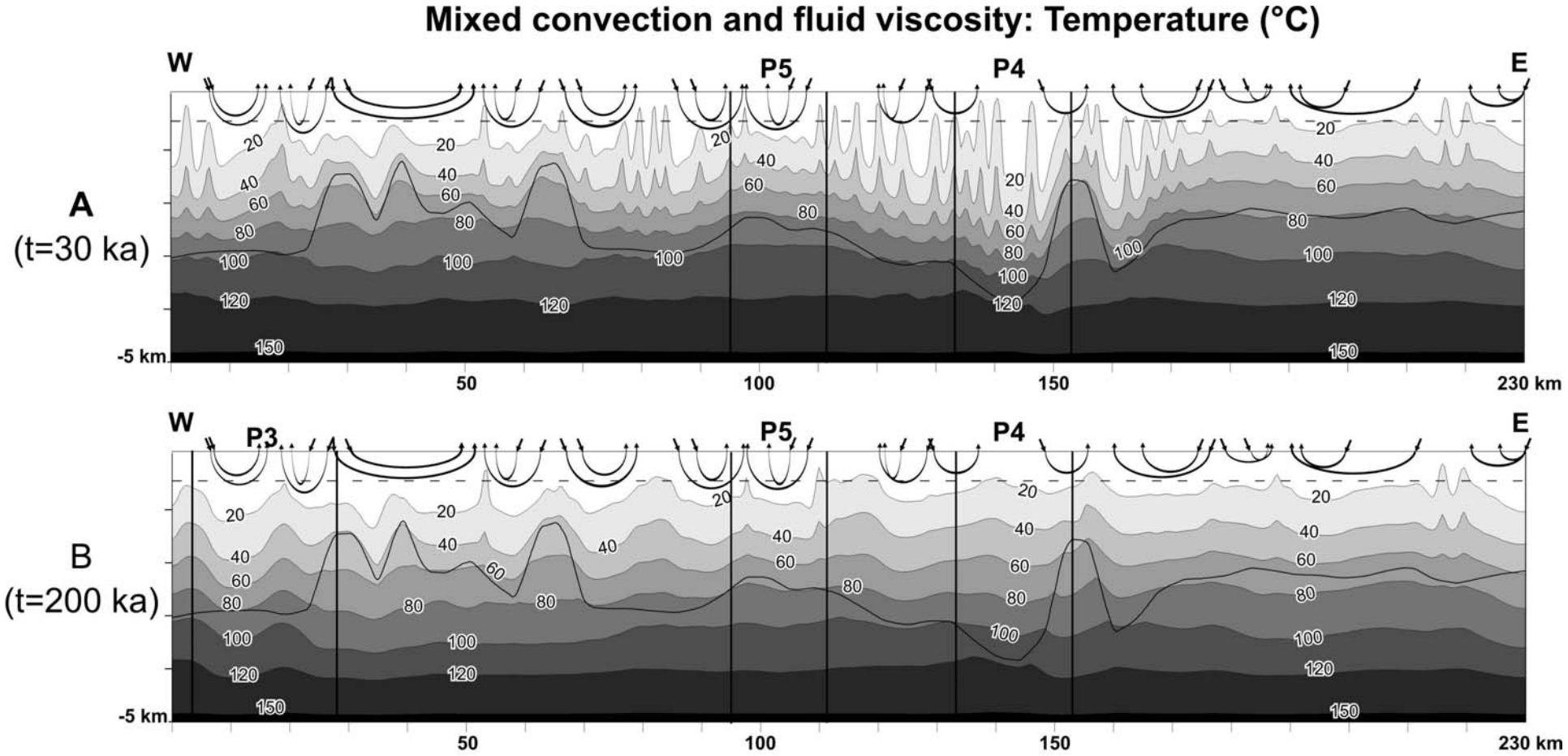

Fig.3-19: A and B: Temperature distribution resulting from mixed convection and viscosity effects at t=30 ka and t=200 ka respectively. Salt concentrations are expressed in g/L. Two profiles P4 and P5 are located within the cross-section. The simulation results for these two profiles are shown with no vertical exaggeration in Fig.3.20 and Fig.3.21

The effects of viscosity on the concentration field are inferred by comparing these patterns with those of the previous simulation in which viscosity dependencies are neglected (Fig.3.13 A, B). Viscosity variation strongly influences the salt concentration profile within the sediments. At early time stages, most of the brine fingers are stretched up to the surface (Fig.3.18 A) suggesting that a more vigorous upward brine flow takes place. As time progresses, the narrow brine fingers evolve in broader brine patterns shaped by the regional flow (Fig.3.18 B). Salty water with more than 2 g/L of dissolved halite spreads at the surface covering the discharge areas. The concentration isopleths are more pulled up when the viscosity is variable. Near the eastern salt diapir, waters with 20 g/L of dissolved halite reach 1 km depth (Fig.3.18B) whereas at constant viscosity these salty waters are embedded in the deeper part of the basin (Fig.3.13B). Furthermore, in the central part of the basin, the brine patterns display closer vertical fronts proving that viscosity variation can promote lateral brine flow as well. This area of the basin denoted by “P 5” will be illustrated in more details afterwards.

At early an time stage, the temperature profile displays oscillatory perturbations (Fig.3.19A) comparable to those observed with constant fluid viscosity (Fig.3.14 A). On the other hand, at the end of the simulation run (Fig.3.19 B), the isotherms are smoothed in association with a layered brine patterns.

Insights into the effects of viscosity on the flow regime are gained by comparing time dependent patterns for profile P4 in which viscosity is either constant (Fig.3.16) or variable (Fig.3.20). In the first case, at the begin of the simulation process, thermally induced brine plumes with 1 g/L of dissolved salt reach a depth of 1.5 km flowing at 0.1 m yr^{-1} (Fig.3.16 A1). On the other hand, at the same time step, when a variable viscosity is taken into account, brine plumes with 1g/L of dissolved salt flow through the surface at rates ranging from 0.2 to 0.4 m yr^{-1} (Fig.3.20 A1). This observation reflects the viscosity effects on the hydraulic conductivity. As previously explained, owing to the temperature dependence of the viscosity, the hydraulic conductivity increases with temperature. Therefore increased hydraulic conductivities occur in direct relation to the increased temperature gradients of the convective regime. Consequently, in these areas, the resulting flow is more intense. To some extent viscosity dependencies introduce permeability heterogeneities within the stratigraphic units of the basin. The sediments are locally more permeable where upward hot brine flows occur and the flow rates of thermally induced brine plumes are further enhanced.

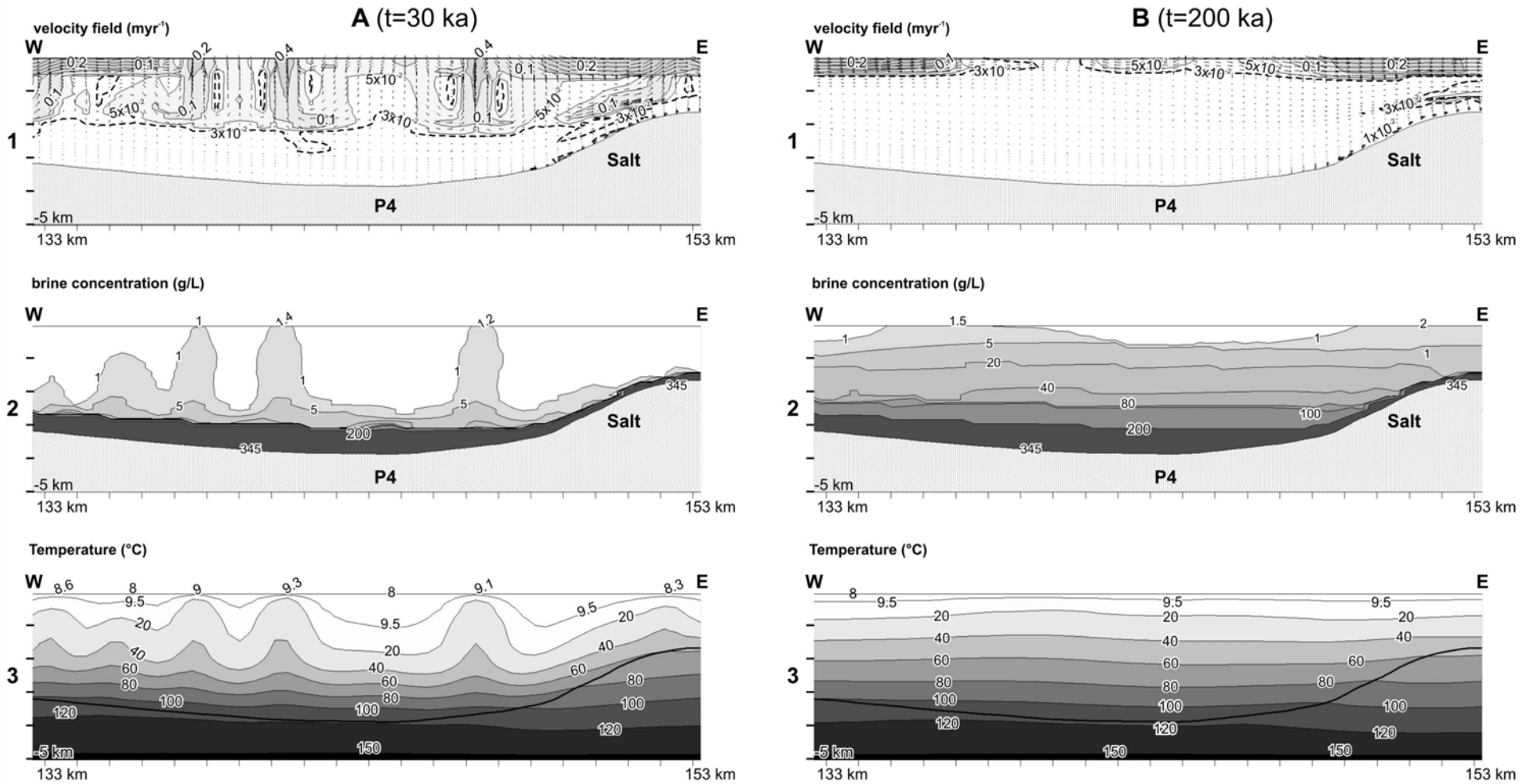

Fig.3-20: A and B: Zoom of the thermohaline simulation results for profile P4 as located in Fig.3.18 at t=30 ka and t=200 ka respectively. No vertical exaggeration is used. **1:** Pore water velocity field in myr^{-1}. Pore vector linearly scaled to the largest flow arrow. **2:** salt concentrations in g/L. **3:** temperature distribution in °C.

By comparing Fig.3.16 A2 with Fig.3.20 A2 it turns out that at the begin of the simulation process, the viscosity does affect the spatial distribution of the brine plumes: finger patterns develop at the same locations. This feature is due to the early temperature oscillatory regime which is the same when viscosity is constant (Fig.3.16 A3) or variable (Fig.3.20 A3).

However, while in a constant viscosity regime the convective regime persists over time (Fig.3.16 B1), with a variable viscosity the convective cells disappear within P4 (Fig.3.20 B1). The velocity field displays broad stagnation areas except in the shallow aquifer where the regional flow takes place, and along the salt diapir flank where a mass Dirichlet boundary condition is set. The very low velocities are due to the high brine concentration values throughout the profile (Fig.3.20 B2). Owing to the intense brine flow rates enhanced by viscosity, as time progresses more saltier and heavier water fills the sediment. Consequently the pore velocities decrease faster. The mass profile evolves in a layered stratification in which concentration increases with depth. Freshwater conditions occur in association with the recharge area in the central part of the profile. Accordingly, the temperature field is slightly disturbed (Fig.3.20 B3).

On the other hand, the convective regime still occurs in the central part of the basin after 200 ka as shown in profile 5 (Fig.3.21). A thermally induced convective cell affects the eastern end of the section (Fig.3.21 1). In relation to the upward flow enhanced by the effects of viscosity, a vertical brine front with 1 g/L of dissolved halite develops adjacent to the west-east regional flow (Fig.3.21 2). As seen by the 0.5 g/L isopleth, a density lid forms at the top of the plume spreading laterally toward the regional flow. Consequently lateral directed brine flow is likely favored in that part of the basin. As more salt fills the sediment, the convective cell will break down and the brine plume will extend toward the center of the profile as it is the case at the western part of the section. This further suggests that the convective regime has not achieved a steady state.

Mixed convection and fluid viscosity: Profile P5

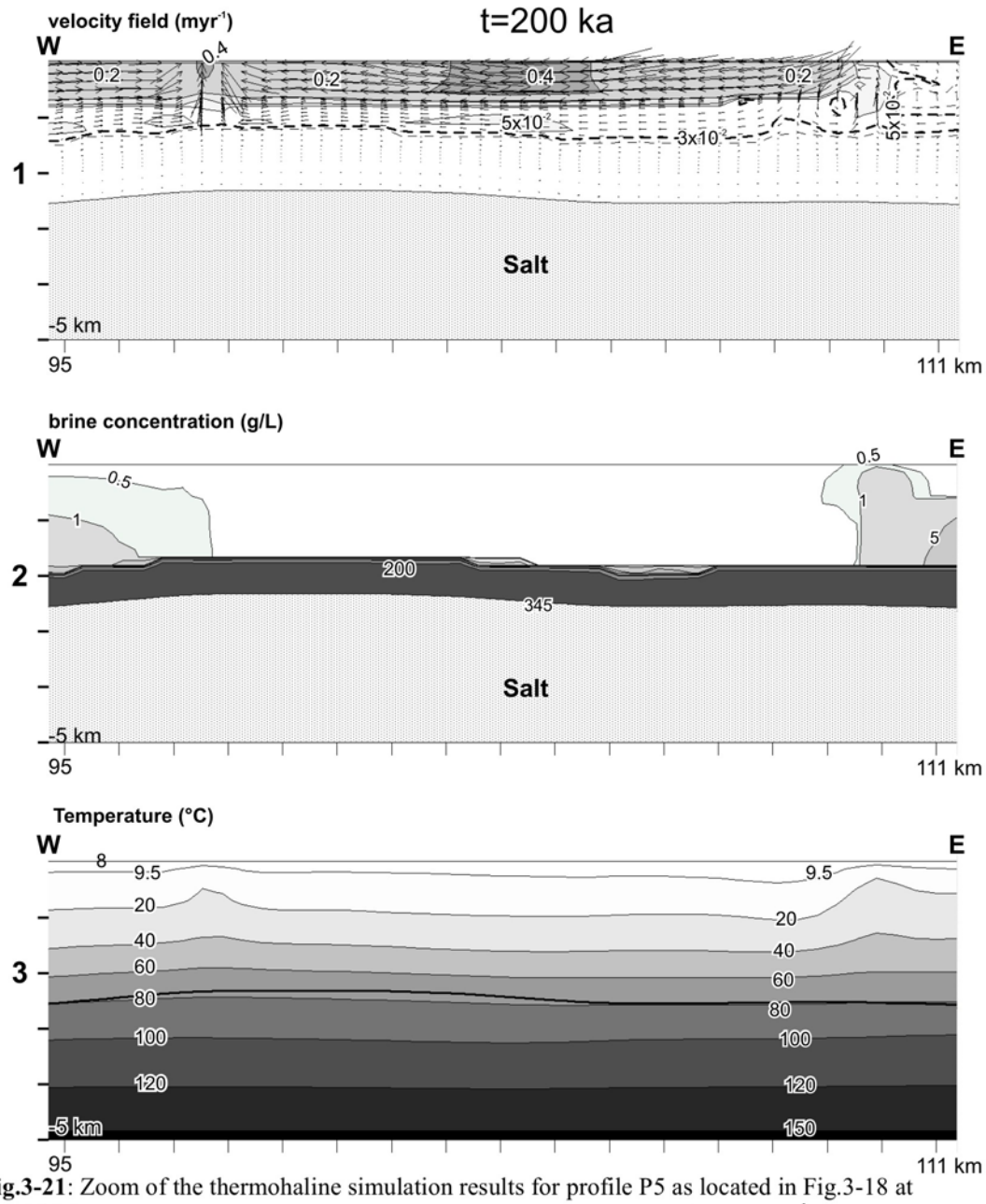

Fig.3-21: Zoom of the thermohaline simulation results for profile P5 as located in Fig.3-18 at $t = 200$ ka . No vertical exaggeration is used. **1:** Pore water velocity field in myr^{-1}. Pore vector linearly scaled to the largest flow arrow. **2:** salt concentrations in g/L. **3:** temperature distribution in °C.

3.3 Discussion

The different types of simulation have highlighted the major components involved in brine transport within the NEGB. Within the Buntsandstein the regime is purely diffusive, i.e. mass concentration increases linearly with depth. The fresh/salt water interface develops up to the Muschelkalk which shapes the brine front owing to its very low permeability. In salt diapir environnents, pure diffusive brine transport is dominant. The large lateral salinity gradients supplied by the salt diapirs induce downward brine flow along the steep salt diapir flanks. The plumes are layered and extend away from the salt domes over 30 km in the lateral directions. In the free thermohaline regime, the flow is self-organized into several cells: their size is controlled by the aquifer thickness, basin geometry and permeability ratios. The thermal induced cells are more vigorous in the shallow aquifer where the layers are more permeable. In salt dome environments, the perturbed temperature field generates thermal buoyant forces stronger than the gravitational field. As a result, solute and thermal fingers develop over the same area and penetrate within the sediment fill up to the surface. The upward brine flow is also present in the sediments overlying steep salt diapirs.

The fundamental importance of temperature effects for surface brine occurrences is directly inferred by comparing the patterns for brine transport and regional flow (Fig.3-5) with those resulting from mixed convection (Fig.3-13). In the first case, the brine leaches through the surface only at the western part of the basin where shallow salt dissolution occurs in association with the strongest discharge flow rates. Throughout the rest of the basin salt upconing does not exceed half a kilometer depth. On the other hand, when the temperature effects are taken into account in the model, the brine patterns develop as salty fingers reaching the surface. The areas likely favored for surface salty water occurrences are the discharge areas (basin lowlands) in which solute and thermal plumes are advected by the regional flow and in flat areas in which the free thermohaline regime is dominant.

Furthermore the simulations have allowed to estimate the effects of viscosity on the velocity, mass, and temperature fields. Owing to the temperature dependence of the viscosity, thermally induced brine plumes flow at increased velocities. Consequently more dissolved halite is transported by the convective regime throughout the basin.